Internal Tides at the Coast: Energy Flux of Baroclinic Tides Propagating into the Deep Ocean in the Presence of Supercritical Shelf Topography

VARVARA E. ZEMSKOVA,[a] RUTH C. MUSGRAVE,[b] AND JAMES A. LERCZAK[a]

[a] *Oregon State University, Corvallis, Oregon*
[b] *Dalhousie University, Halifax, Nova Scotia, Canada*

(Manuscript received 14 August 2023, in final form 16 February 2024, accepted 4 March 2024)

ABSTRACT: The generation of internal tides at coastal margins is an important mechanism for the loss of energy from the barotropic tide. Although some previous studies attempted to quantify energy loss from the barotropic tides into the deep ocean, global estimates are complicated by the coastal geometry and spatially and temporally variable stratification. Here, we explore the effects of supercritical, finite amplitude bottom topography, which is difficult to solve analytically. We conduct a suite of 2D linear numerical simulations of the barotropic tide interacting with a uniform alongshore coastal shelf, representing the tidal forcing by a body force derived from the vertical displacement of the isopycnals by the gravest coastal trapped wave (of which a Kelvin wave is a close approximation). We explore the effects of latitude, topographic parameters, and nonuniform stratification on the baroclinic tidal energy flux propagating into the deep ocean away from the shelf. By varying the pycnocline depth and thickness, we extend previous studies of shallow and infinitesimally thin pycnoclines to include deep permanent pycnoclines. We find that scaling laws previously derived in terms of continental shelf width and depth for shallow and thin pycnoclines generally hold for the deeper and thicker pycnoclines considered in this study. We also find that baroclinic tidal energy flux is more sensitive to topographic than stratification parameters. Interestingly, we find that the slope of the shelf itself is an important parameter but not the width of the continental slope in the case of these steep topographies.

SIGNIFICANCE STATEMENT: The objective of this study is to better understand how vertical density stratification, which can vary seasonally in the ocean, affects the interaction of tides with steep coastal topography and the generation of waves that travel away from the coast in the ocean interior. These waves in the interior can travel over long distances, carrying energy offshore into the deep ocean. Our results suggest that the amount of energy in these internal waves is more sensitive to changes in topography and latitude than to the vertical density profile. The scaling laws found in this study suggest which parameters are important for calculating global estimates of the energy lost from the tide to the ocean interior at the coastal margins.

KEYWORDS: Ocean; Continental shelf/slope; Internal waves; Tides; Mass fluxes/transport; Numerical analysis/modeling

1. Introduction

Astronomically driven barotropic tides lose part of their energy to baroclinic internal tides when they interact with topography in the presence of stratification (Bell 1975; Baines 1982). These internal tides can propagate large distances (thousands of kilometers) away from the topography to where they can play an important role in mixing density and momentum (Alford 2003; Kunze et al. 2012; MacKinnon et al. 2017). Their dissipation away from the generation site results in ocean mixing that is thought to contribute to sustaining abyssal stratification and overturning circulation (Munk and Wunsch 1998; Wunsch and Ferrari 2004) with mixing enhanced by rough bottom topography driving downwelling and sloping topography playing an important role for along-slope upwelling (Ferrari et al. 2016; Drake et al. 2022). As their vertical displacements in the interior can be quite large, they are also important for distributing nutrients (Stevens et al. 2012; Tuerena et al. 2019). In this study, we specifically focus on the superinertial tides. In many parts of the ocean, the semidiurnal (M_2) tide, which is superinertial equatorward of 74.5°, propagates along a coastline as a zero mode (Huthnance 1978). Modes here refer to coastal modes, with higher modes having more zero crossings in the cross-shore direction; as such, the zero, or the gravest, mode has no zero crossings and is vertically uniform. The gravest mode against a nonvertical coast is sometimes called a topographically modified Kelvin wave, to account for the deviations from the Kelvin wave structure defined at a vertical wall. The deviations associated with the gravest coastal mode from a Kelvin wave are what generate the internal tides that we discuss in this paper. Interest in this interaction of the tide with coastal topography and generation of baroclinic tides can be traced back to Rattray (1960, 1969), Huthnance (1975, 1978, 1981), Mysak (1980), and Chapman and Hendershott (1982).

Internal tide generation over isolated ridges in the open ocean has been extensively studied in the past (Garrett and Kunze 2007, and references therein). Llewellyn Smith and Young (2003) derived an analytical expression for the energy flux of the internal tides generated by tidal flow over a knife-edge ridge (an idealized representation of steep topography) in the case of uniform stratification. In this expression, energy flux radiating away from the topography is proportional to

Corresponding author: Varvara E. Zemskova, barbara.zemskova@oregonstate.edu

DOI: 10.1175/JPO-D-23-0164.1

the barotropic velocity squared, height of the ridge, and parameter $\sqrt{\omega^2 - f^2}$, where ω is the tidal frequency and f is the Coriolis frequency. In a similar analysis to step topography, St. Laurent et al. (2003) found the knife-edge ridge approximation to be a good model for abrupt topography, which can be used as a prototype for coastal shelf topography. In both models, the dependence of energy flux on latitude, i.e., f, arises due to the dependence of the group speed (comes from the dependence of the horizontal wavenumber of the generated waves and hence their group speed) on $\sqrt{\omega^2 - f^2}$ (Kelly et al. 2013).

St. Laurent et al. (2003) also derived that the baroclinic energy flux is proportional to the square of barotropic velocity u_{bt}^2 for step topography. This is because at the step, the velocity of the internal tides radiating away from the step must be matched to be proportional to the barotropic velocity (St. Laurent et al. 2003), and the baroclinic energy flux is proportional to the square of internal tide velocity (Kelly et al. 2013). By representing arbitrarily sloping topography with a collection of steps, and matching flat bottom modes between each step so that energy is conserved, Kelly et al. (2013) found similar scalings for the baroclinic energy flux of internal tides radiating away from the sloping topography.

However, the problem of internal tide generation at steep ridges or infinitely wide step topography is different from tidal generation at continental slopes in three important ways. First, continental shelves are typically much shallower and can be substantially wider than the oceanic ridges for which the previously derived scalings are appropriate. Second, the depth-averaged cross-bathymetric currents are different at the coast from those in the open ocean. This is important to consider for imposing a barotropic forcing in a 2D model, especially as in ridge or infinitely wide step-topography models, barotropic forcing is imposed at the open-ocean end. This point is further discussed in section 4. Finally, models of flows over oceanic ridges and infinitely wide step topography assume radiating boundary conditions on both sides of the domain, allowing the energy to radiate away from the topographic obstacle in both directions. However, the coast is often modeled using a no-flow boundary condition (zero cross-shore velocity) (Hall et al. 2013; Zhang and Yankovsky 2016), which may lead to dynamical differences compared to the radiative boundary conditions. For example, Kelly et al. (2013) found that when a vertical wall was imposed at the coast (i.e., shelf width was finite), the baroclinic energy conversion was sensitive to the shelf width in the case of mode-1 internal tide incident on the coast. An argument can also be made that the radiative boundary condition accounts for the dissipation of energy in turbulent shallow waters at the coast. Yet, observations of standing internal tides on continental shelves (Lerczak et al. 2003; Rayson et al. 2012; Suanda and Barth 2015) point to some energy being reflected from the coast. Overall, it cannot be a priori be concluded that the scalings derived in ridge and step-topography models would hold for tidal generation over the continental shelf topography in nonuniform stratification, a point that we investigate in our study.

Numerous previous studies showed that the generation and propagation of baroclinic tides are sensitive to the shape of the topography (Baines 1973; Craig 1987). One of the relevant parameters that has been identified is the topographic criticality. It is defined as

$$\alpha = \left| \frac{\nabla h}{\sqrt{(\omega^2 - f^2)/(N_{\text{bot}}^2 - \omega^2)}} \right|, \tag{1}$$

and it represents the ratio of topographic slope $\nabla h(x, y)$, where $h(x, y)$ is the local depth, to the characteristic slope of an baroclinic tide, and where N_{bot}^2 is the squared buoyancy frequency along the bottom. We define α_{max} to be the maximum value within the domain. Topography is considered to be subcritical if $\alpha_{\text{max}} < 1$ and supercritical if $\alpha_{\text{max}} > 1$. Subcritical topography generates beams that propagate upward away from the generation region on the continental slope (Bell 1975). For critical slopes ($\alpha_{\text{max}} \to 1$), the generated beam is along the slope such that nonlinear effects become important, leading to local wave breaking and dissipation (Dauxois et al. 2004; Gayen and Sarkar 2011b). Supercritical topography generates beams that propagate both upward and downward away from the shelf (Llewellyn Smith and Young 2003). The topographic criticality parameter α_{max} has been previously used to scale baroclinic energy flux away from the topography. Previous studies found that the energy flux magnitude increases with α_{max} (Sherwin and Taylor 1990; Kelly et al. 2010), at a higher rate for subcritical topographies [e.g., scaling as $\propto \alpha^5$ for subcritical and $\propto \alpha$ for supercritical topographies in Craig (1987)].

Stratification can also affect the conversion of barotropic to baroclinic tidal energy, especially as seasonal cycles in maximum stratification can change α_{max} (Cacchione et al. 2002). For example, observational work by Liu et al. (2019) found that in the Yellow Sea, baroclinic energy fluxes were larger in the summer, when maximum N^2 was greater, compared with winter, when water was more well mixed. Using ray tracing, Baines (1982) derived analytical expressions to compute energy flux radiated away from either subcritical or supercritical topographies for a given topographic geometry and stratification and provided a global estimate of baroclinic energy flux from internal tides generated at the coast. It is important to note that both our model presented here and the analytical expressions in Baines (1982) are inviscid, such that the dissipation rate is zero and the barotropic-to-baroclinic energy conversion is exactly equal to the divergence of the outgoing energy flux. However, estimates by Baines (1982) assumed a shallow pycnocline, which may not be the case in some parts of the ocean (Sherwin and Taylor 1990; Stewart and Thompson 2016; Barbot et al. 2021). It also assumed an infinitely thin pycnocline that transitioned from a well-mixed top layer into a linearly stratified bottom layer. Yet, pycnocline thickness is finite, and its depth can vary significantly, for instance, from around 200 m deep along the Australian North West Shelf (Rayson et al. 2019) to 459 m deep in the East China Sea (Vieira and Allshouse 2020) to up to 1 km deep in the Bay of Biscay (Barbot et al. 2021). Feucher et al. (2019) found that permanent pycnoclines can be quite deep and thick; particularly along the eastern boundary of the North Atlantic, the

mean depth and thickness of the pycnoclines are about 750 and 400 m, respectively. The importance of nonuniform stratification to tide-topography interaction has been previously studied (Nash et al. 2004; Hall et al. 2013), though these studies were not specifically focused on the internal tide generation. Gerkema et al. (2004) found that a deep and thick permanent pycnocline in the Bay of Biscay plays a role in determining baroclinic energy conversion rates. Furthermore, Gerkema and van Haren (2012) found that spatially nonuniform stratification changes generated internal tide beams in channel simulations. More recently, Hartharn-Evans et al. (2022) showed that the shoaling of baroclinic tides propagating onto a shelf may be sensitive to pycnocline thickness.

However, to our knowledge, sensitivity of energy flux of the internal tides generated by the interaction of the barotropic tide with coastal topography to the shape of the pycnocline has not been systematically examined; hence, it is the aim of this study. We take a two-dimensional linear model with the coast at one boundary and the open ocean the other. The model is highly idealized—it is inviscid, linear, neglects alongshore variations, and uses simplified analytical expression for bottom topography. However, such simplifications allow us to calculate energy fluxes over a large parameter space (pycnocline depth and thickness, topographic parameters, and latitude) using significantly less computational resources than would be required of more realistic, but computationally expensive, ocean circulation models. Recent efforts to study the generation of internal tides at steep topography have also used Green's functions (Griffiths and Grimshaw 2007; Lahaye and Llewellyn Smith 2020) or local eigenfunction expansions (Papoutsellis et al. 2023). However, in their current numerical formulation, these models are limited to uniform stratification, whereas our model can readily take any vertically nonuniform stratification profile and is, thus, better suited to address the goals of this study.

As baroclinic internal tide beams generated at the continental slope with energy flux traveling offshore, they further reflect off the bottom becoming upward propagating and then again off the surface becoming downward propagating and repeating the pattern (Craig 1987; Lamb 2014). The pycnocline can also play an important role in the propagation of the baroclinic tide modes (Baines 1982; Gerkema 2001), which we will examine here. The stratification affects the shape of the vertical modes and their speeds; however, in a linear model, we neglect the solitary wave generation, which is sensitive to stratification as shown in Gerkema (2001). Our setup is similar to previous studies of internal tide generation on the continental slope (Sherwin and Taylor 1989; Dale and Sherwin 1996; Klymak et al. 2016). We will focus our analysis on the amount of baroclinic energy flux from internal tide generation at the continental shelf that is radiated into the deep ocean. As we are interested in the barotropic-to-baroclinic energy conversion, our model will be forced by the barotropic tide body force, rather than incident mode-1 baroclinic tide used in other previous studies that did not consider the generation process itself (e.g., Hall et al. 2013; Wang et al. 2018). The approximation for the body force used in this study was derived in Baines (1973) and previously used to calculate baroclinic energy fluxes (e.g., Sherwin and Taylor 1990; Morozov 1995; Sherwin et al. 2002; Gerkema et al. 2004). Despite this idealized setup, the superinertial tidal forcing (M_2 tide is superinertial equatorward of 74.5°), supercritical coastal topography that is ubiquitous in the ocean (Lamb 2014), and nonuniform stratification make the numerical approach challenging, in particular requiring high horizontal and vertical resolutions, which we will discuss in this paper.

This paper is organized as follows. In section 2, we detail the setup of the numerical simulations (topography, stratification), governing equations (coupled u–p equations), and the Baines body forcing. In section 3, we explain our numerical methodology to solve the governing equations using finite differences (section 3a) and examine the numerical convergence of the solution, which is complicated by the hyperbolic nature of the governing equations (because $\omega > f$), nonuniform stratification, and the Σ-coordinate system (section 3b). We then compare the solutions of our model with two existing linear internal tide models in section 4. Sensitivities of baroclinic energy flux magnitude to stratification, latitude, and topography are presented in sections 5a–5c, comparing our results to the previously derived scalings (Llewellyn Smith and Young 2003; St. Laurent et al. 2003) and analytical expression derived by Baines (1982). Appropriate scaling for baroclinic energy flux magnitude is presented in section 5d. Finally, section 6 summarizes and connects our results to oceanographic observations.

2. Setup and governing equations

The simulation setup that we consider in this study is shown in Fig. 1a. The domain of interest has coastal topography of depth $h(x)$ steeply sloping nearshore, and a large portion of the domain is flat with a depth H. The across-shore (x) extent of the domain is taken to be $[-L_x, 0]$, such that the coastal boundary is at $x = 0$ and the open ocean boundary is at $x = -L_x$. The bottom topography is uniform in the alongshore (y) direction. We also impose background stratification $N(z)$ that is horizontally uniform.

In our simulations, we prescribe bottom topography to be

$$h = -H, \text{ for } x < -(x_s + x_W), \tag{2}$$

$$h = -h_s - (H - h_s)\left(0.5\left\{1 - \cos\left[\frac{\pi(x + x_s)}{x_W}\right]\right\}\right)^{0.75}, \quad \text{for } -(x_s + x_W) < x < -x_s, \tag{3}$$

$$h = \frac{h_s - h_c}{x_s}x - h_c, \text{ for } x > -x_s, \tag{4}$$

where H is the maximum depth at the flat offshore potion of the domain, h_c is the depth at the coast, h_s is the depth at the shelf break, x_s is the shelf width, and x_w is the slope width. For our baseline simulations, we set $H = 3.1$ km, $h_c = 100$ m, $h_s = 150$ m, $x_s = 80$ km, and $x_W = 32$ km. We take the domain size to be $L_x = 300$ km in order to allow for a sufficiently flat

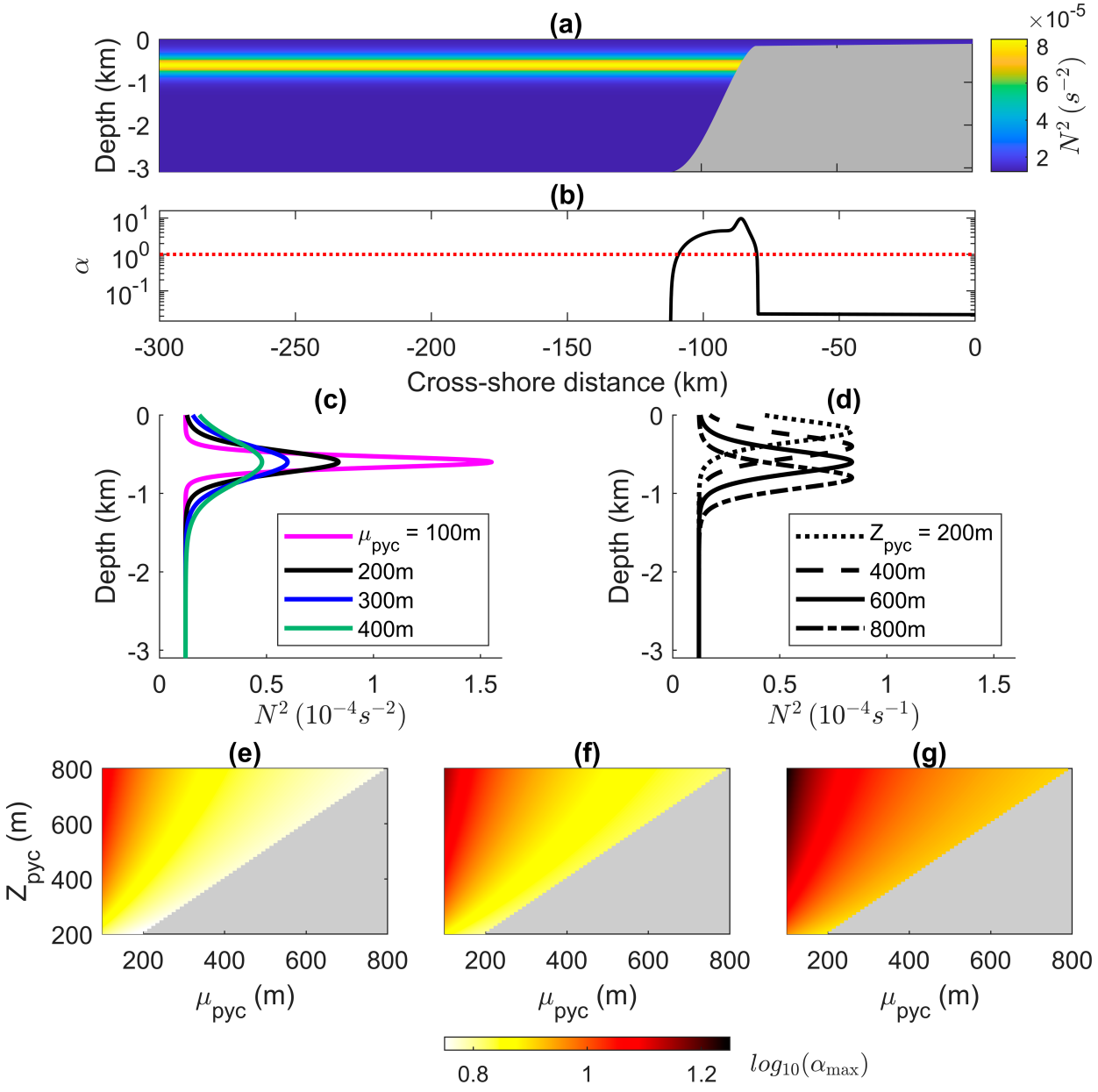

FIG. 1. (a) Domain setup showing the topography (continental shelf, slope, and the deep region) with overlaid color indicating sample stratification with pycnocline thickness $\mu_{pyc} = 200$ m and depth $Z_{pyc} = 600$ m; (b) topographic criticality parameter α for $f = 0.93 \times 10^{-4}$ s^{-1} and $\omega = \omega_{M_2} = 1.41 \times 10^{-4}$s^{-1} and the same pycnocline as in (a) with dotted line marking $\alpha = 1$; note that in the deep region, $\alpha = 0$, so it does not appear on a log plot; (c) stratification profile varying pycnocline thickness set at depth of 600 m; (d) stratification profiles varying pycnocline depth set at thickness of 200 m; and (e)–(g) α_{max} as a function of stratification depth and thickness computed with $f = 0.73 \times 10^{-4}$ s^{-1} (~30°), $f = 0.93 \times 10^{-4}$ s^{-1} (~40°), and $f = 1.11 \times 10^{-4}$ s^{-1} (~50°), respectively.

open ocean region. This piecewise topography follows the idealized topography used in Dale et al. (2001) and is similar to the one used in other previous studies of the interactions of tides with coastal topography (e.g., Klymak et al. 2016; Zhang and Yankovsky 2016). This functional form of the topography allows us to control for the maximum value of the slope through parameters x_W and h_s in Eq. (3). In many previous studies (e.g., Legg and Adcroft 2003; Kelly and Nash 2010; Hall et al. 2013), the shelf has been commonly assumed to be flat, i.e., $h_c = h_s$. However, as shown in two realistic profiles from ocean bathymetry [General Bathymetric Chart of the Ocean (GEBCO) Compilation Group 2020] in Fig. 2, there is often a slight slope on the continental shelf itself. For example, for the selected profiles, $h_s = 165$ m and $h_c = 83$ m off the eastern coast of South America and $h_s = 78$ m and $h_c = 35$ m off the western coast of Australia. We will test whether the

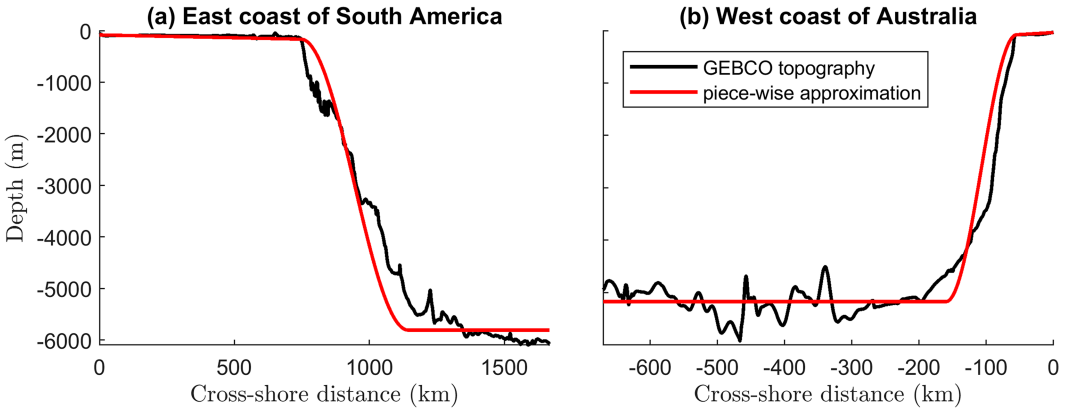

FIG. 2. Depth profiles as a function of cross-shore distance from GEBCO (black lines) and piecewise fit in the form using Eqs. (2)–(4) (red lines) for sample bathymetries off the (a) eastern coastline of South America and (b) western coastline of Australia.

shelf slope affects the magnitude of baroclinic energy flux by considering both $h_c \neq h_s$ and $h_c = h_s$ in section 5c.

We prescribe buoyancy frequency squared to be

$$N^2 = N_{\text{bg}}^2 + \frac{\rho_2 - \rho_1}{\rho_0}\frac{g}{\mu_{\text{pyc}}}\left[\text{sech}\left(\frac{z - Z_{\text{pyc}}}{\mu_{\text{pyc}}}\right)\right]^2, \tag{5}$$

where ρ_1 and ρ_2 are the densities of upper and lower layers, respectively; background density is $\rho_0 = 0.5(\rho_1 + \rho_2)$, μ_{pyc} is the pycnocline thickness; Z_{pyc} is the pycnocline depth, and N_{bg}^2 is the constant buoyancy frequency squared associated with background linear density gradient. For all simulations, we set $\rho_1 = 1027$ kg m^{-3}, $\rho_2 = 1030$ kg m^{-3}, and $N_{\text{bg}}^2 = 1.22 \times 10^{-5}$s^{-2}. In the majority of our simulations, the pycnocline is below the shelf break, with the exception of some simulations in section 5c, where we vary the value of h_s allowing it to be deeper than Z_{pyc}.

As shown in Fig. 1 for an example stratification with pycnocline depth of 600 m and thickness of 200 m, the topography is supercritical ($\alpha > 1$) in the continental slope and shelfbreak regions and subcritical ($\alpha < 1$) in the deep region and on the shelf with respect to the baroclinic tide characteristic, with α defined in Eq. (1). In this study, we primarily examine $f = 0.93 \times 10^{-4}$ s^{-1}, which is representative of the Coriolis parameter at midlatitudes (~40°). However, we also extend our analysis to examine the dynamics over a range of latitudes 20°–67.8° ($f = 0.5$–1.35×10^{-4} s^{-1}). We consider the M_2 tidal frequency ($\omega = 1.41 \times 10^{-4}$ s^{-1}). In this study, we will vary pycnocline thickness and depth across numerical simulations as shown in Figs. 1c–g. As we increase the pycnocline thickness (cf. Fig. 1c), the peak value of N^2 decreases to maintain the difference in ρ across the pycnocline. From Eq. (1), for a fixed topographic slope and fixed forcing frequency ω, α_{max} increases with increasing latitude, i.e., greater f (cf. Figs. 1e–g). The stratification profile also affects α_{max}; because max(N^2) increases with decreasing pycnocline thickness (Fig. 1c), α_{max} is larger for thinner pycnoclines. The location of max(N^2) with respect to the maximum topographic slope changes with pycnocline depth; hence, α_{max} depends on Z_{pyc} as well as μ_{pyc} (Figs. 1e–g). We will also change topography through x_s, h_s, h_c, and x_W, some of which will change α_{max}.

We consider the Boussinesq approximation of the incompressible, rotating, inviscid Navier–Stokes equations. The linearized governing equations for the baroclinic internal waves are

$$\frac{\partial u'}{\partial t} - fv' = -\frac{1}{\rho_0}\frac{\partial p'}{\partial x}, \tag{6}$$

$$\frac{\partial v'}{\partial t} + fu' = -\frac{1}{\rho_0}\frac{\partial p'}{\partial y}, \tag{7}$$

$$\frac{\partial w'}{\partial t} = -\frac{1}{\rho_0}\frac{\partial p'}{\partial z} - \frac{g\rho'}{\rho_0} + F, \tag{8}$$

$$\frac{\partial \rho'}{\partial t} - \frac{\rho_0 N^2}{g}w' = 0, \tag{9}$$

$$\frac{\partial u'}{\partial x} + \frac{\partial v'}{\partial y} + \frac{\partial w'}{\partial z} = 0, \tag{10}$$

where $\mathbf{u}' = (u', v', w')$ is the velocity vector in (x, y, z) directions; p' is the pressure; ρ' is the density, all of which are fluctuations associated with the baroclinic waves; and F is the forcing, which will be discussed below. From the system of Eqs. (6)–(10), we derive coupled equations for u' and p' subject to boundary conditions, implementing assumptions from Baines (1982). Equations from Baines (1982) are rederived in this form, rather than in the streamfunction form presented in the original study, in order to facilitate the theoretical and numerical comparisons with the Dale et al. (2001) model. Furthermore, we retain the nonhydrostatic term in the governing equations presented in Dale and Sherwin (1996), Dale et al. (2001), and Garrett and Gerkema (2007).

a. *Coupled u′–p′ equations*

We assume that the perturbations, i.e., baroclinic motions, are of the following plane waveform:

$$(u', v', w', p', \rho') = [\hat{u}'(x, z), \hat{v}'(x, z), \hat{w}'(x, z), \hat{p}'(x, z), \hat{\rho}'(x, z)]e^{-i\omega t + ily}, \tag{11}$$

where ω is a tidal frequency and l is the alongshore wavenumber. In this study, we will follow the assumption by Baines (1982) that the alongshore wavelength is much longer than the baroclinic scales of interest and therefore assume that $l = 0$.

Using the form of baroclinic perturbations in Eq. (11) and the linearized governing Eqs. (6)–(10), we derive the following coupled u'–p' equations with $\tilde{F}$ being the forcing term:

$$\frac{1}{\rho_0}\frac{\partial \hat{p}'}{\partial x} + \frac{\omega^2 - f^2}{i\omega}\hat{u}' = 0, \tag{12}$$

$$\frac{1}{\rho_0}\frac{\partial^2 \hat{p}'}{\partial z^2} - \frac{1}{N^2 - \omega^2}\frac{dN^2}{dz}\frac{1}{\rho_0}\frac{\partial \hat{p}'}{\partial z} + \frac{N^2 - \omega^2}{i\omega}\frac{\partial \hat{u}'}{\partial x} = \tilde{F}. \tag{13}$$

The relationship between F in Eq. (8) and $\tilde{F}$ in Eq. (13) will be discussed below. We keep the nonhydrostatic terms in Eqs. (12) and (13) because they may become important in the deeper regions of the domain, where the stratification is weak. For simplicity, we will be dropping hats for $\hat{u}'$ and $\hat{p}'$ for the remainder of the paper.

We impose coastal wall boundary condition,

$$u' = 0 \quad \text{at} \quad x = 0, \tag{14}$$

rigid-lid boundary condition at the surface, such that

$$\frac{\partial p'}{\partial z} = 0 \quad \text{at} \quad z = 0, \tag{15}$$

and no flow through the bottom boundary, such that

$$\frac{i\omega}{\rho_0(N^2 - \omega^2)}\frac{\partial p'}{\partial z} + u'\frac{\partial h}{\partial x} = 0 \quad \text{at} \quad z = -h(x). \tag{16}$$

Offshore at the flat-bottom open ocean end, away from the localized forcing at the coast, we assume that the solution can be decomposed as a linear combination of flat-bottom baroclinic modes that are either evanescent or propagating out of the domain (oceanward). The boundary condition for p' can be derived by plugging in such linear decomposition,

$$p' = \sum_{m=1}^{\infty} a_m p'_m(z) e^{ik_m x}, \tag{17}$$

into the unforced second-order equation for p', which is

$$\frac{\partial^2 p'}{\partial z^2} - \frac{1}{N^2 - \omega^2}\frac{dN^2}{dz}\frac{\partial p'}{\partial z} - \frac{N^2 - \omega^2}{\omega^2 - f^2}\frac{\partial^2 p'}{\partial x^2} = 0. \tag{18}$$

It yields an eigenvalue problem for each vertical mode $p'_m(z)$ with eigenvalue k_m to be solved in order to find the offshore boundary condition:

$$\left(\frac{\partial^2}{\partial z^2} - \frac{1}{N^2 - \omega^2}\frac{dN^2}{dz}\frac{\partial}{\partial z}\right)p'_m = -k_m^2\left(\frac{N^2 - \omega^2}{\omega^2 - f^2}\right)p'_m. \tag{19}$$

Signs of the eigenvalues k_m are chosen such that energy flux is outward (out of the domain) at this boundary or decays exponentially offshore in the case of the evanescent modes (Dale and Sherwin 1996; Dale et al. 2001).

b. Forcing term

In Baines (1982), baroclinic motions are assumed to be driven by the body force $\mathbf{F}$, which only has a component in vertical direction. This body force is due to the motions of the gravest mode tide vertically displacing the background density field, i.e.,

$$\mathbf{F} = F\mathbf{z} = -\frac{w_b N^2}{i\omega}\mathbf{z}, \tag{20}$$

where $\mathbf{z}$ is a unit vector in the upward z direction. Here, $w_b = -zQ(1/h)_x$ (Q is the barotropic volume flux) is the vertical velocity of the barotropic motions, approximating the sea surface moving up and down as the barotropic tide comes on and off the shelf. This force is derived for a hydrostatic barotropic tide interacting with a two-dimensional topography (i.e., no variation in y) to be

$$\mathbf{F} = F(x, z)\mathbf{z} = -\frac{g\rho_b}{\rho_0}\mathbf{z} = -\frac{QN^2 z}{\omega h^2}\frac{\partial h}{\partial x}\mathbf{z}. \tag{21}$$

Volume flux Q has been approximated as $Q = \omega\eta x_s$ by Baines (1973), where η is the surface elevation of the barotropic tide and x_s is the shelf width [cf. Eqs. (2)–(4)]. The approximation for the mass flux is derived from the conservation of volume of water as the barotropic tide enters or leaves the coastal shelf. Baines (1982) suggests that this approximation is valid at the scales of baroclinic tide generation (~100 km) as the mass flux of the barotropic tide on the shelf varies on much larger alongshore scales due to its long wavelength. Here, we take $\eta = 0.1$ m, making our Baines body force perhaps smaller than barotropic tide that often has surface elevation of approximately 1 m at the coast.

We apply the forcing from Eq. (21) as $F(x, z)e^{-i\omega t}$ to Eq. (8) and derive the coupled u'–p' system of equations as explained above. Using this Baines body force, the forcing term in Eq. (13), which we solve numerically, becomes

$$\tilde{F}_B(x, z) = \frac{\partial F}{\partial z} - \frac{1}{N^2 - \omega^2}\frac{dN^2}{dz}F. \tag{22}$$

This forcing function depends on both stratification and the shape of bottom topography. It also depends on the forcing frequency, but notably, it is independent of the latitude, i.e., the value of f. Figure 3 shows the examples of the forcing term $\tilde{F}_B(x, z)$ for different pycnocline depths and thicknesses. The $\tilde{F}_B(x, z)$ always has larger values near the shelf break. However, the spatial distribution and magnitude depend on the stratification profile, i.e., both maximum N^2 (cf. Figs. 1c,d) and the depth at which the pycnocline intercepts the topography. As such, the maximum magnitude of $\tilde{F}_B(x, z)$ is a nonlinear function of the pycnocline depth and thickness as shown in Fig. 4a and is explained below.

In the hydrostatic limit ($N^2 \gg \omega^2$), which is largely satisfied for our simulations, the forcing term is simplified to

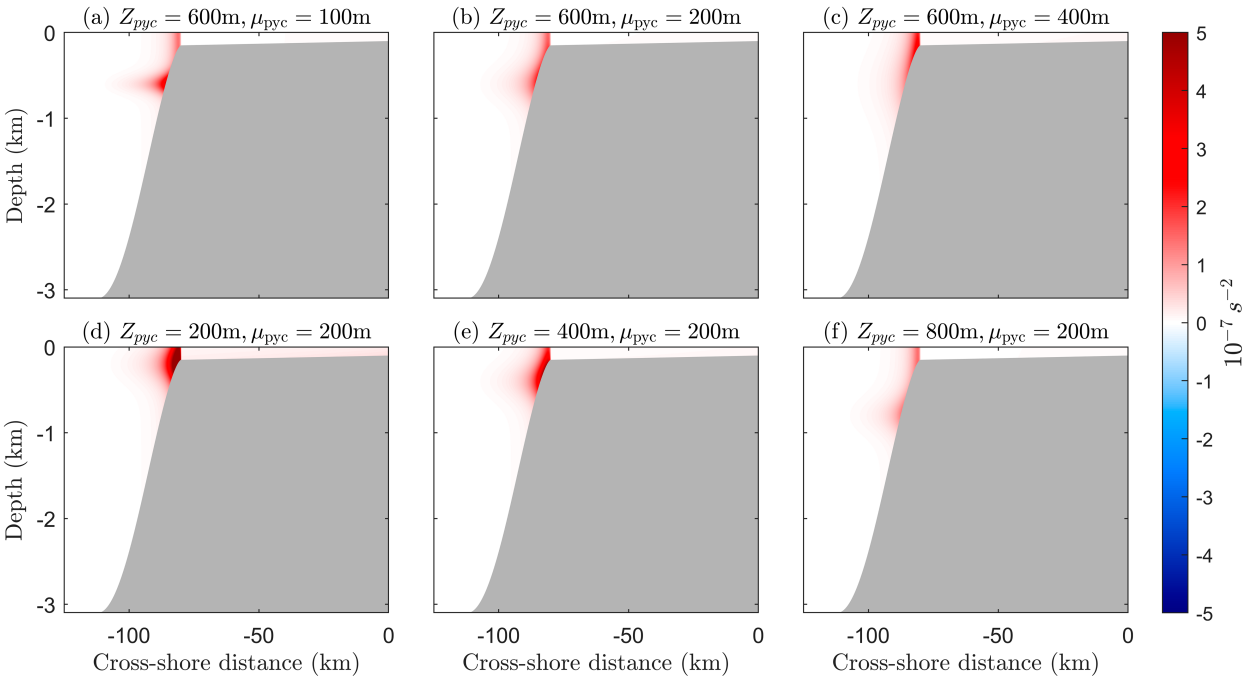

FIG. 3. Comparison of forcing functions $\tilde{F}_B$ for M_2 tidal forcing: (a) pycnocline depth of 600 m, thickness of 100 m; (b) pycnocline depth of 600 m, thickness of 200 m; (c) pycnocline depth of 600 m, thickness of 400 m; (d) pycnocline depth of 200 m, thickness of 200 m; (e) pycnocline depth of 400 m, thickness of 200 m; and (f) pycnocline depth of 800 m, thickness of 200 m. In all cases, forcing functions are predominantly confined to the shelfbreak region, so we do not show the full domain ($x \in [-300\ \text{km}, 0]$) as $\tilde{F}_B = 0$ elsewhere.

$$\tilde{F}_B(x, z) = \frac{QN^2}{\omega h^2}\frac{\partial h}{\partial x}. \tag{23}$$

Maximum N^2 is smaller for thicker pycnoclines (cf. Fig. 1c), and so the maximum magnitude of forcing in general decreases with the thickness of the pycnocline for a given topographic slope and pycnocline depth. However, deeper pycnoclines may be intercepting the topography substantially far away from the shelf break. As a result, the location and the maximum value of the forcing are determined by two competing terms in Eq. (23): N^2 and h_x/h^2 (here and throughout the paper, we use a shorthand notation for derivatives, e.g., $h_x = dh/dx$). We show how the relative importance of these two terms changes with pycnocline thickness in Fig. 4b for a selected pycnocline depth of 600 m by computing the product $N^2_{\rm bot}h_x/h^2$ as a function of cross-shore distance. The stratification along the bottom, $N^2_{\rm bot}$, is maximum at the cross-shore distance where the pycnocline intercepts the topography, and the magnitude of $N^2_{\rm bot}$ is larger for thinner pycnoclines. The other term h_x/h^2 is always largest near the shelf break. Notably, there are two peaks: one that corresponds to where the pycnocline intersects the topography (large N^2) and the second that is at the shelf break (large h_x/h^2). This is true for the simulations in our setup, where we assume that the pycnocline is below the shelfbreak depth. In general, we observe two regimes, depending on which peak is larger. In the first one, for thinner pycnoclines (e.g., $\mu_{\rm pyc} = 100$ m), $\tilde{F}_B \propto N^2_{\rm bot}h_x/h^2$ decreases with increasing pycnocline thickness $\mu_{\rm pyc}$, and the cross-shore location of the maximum value is closer to where the pycnocline intersects the topography. In the second regime (e.g., $\mu_{\rm pyc} = 450$ m), for pycnoclines thicker than some cutoff thickness, $\tilde{F}_B \propto N^2_{\rm bot}h_x/h^2$ increases with increasing $\mu_{\rm pyc}$, and the maximum value of the forcing is around the shelf break. This behavior of the forcing function was not captured by Baines (1982), who only considered thin pycnoclines that are shallower than the continental shelf and thus concluded that the forcing function is always maximized around the shelf break.

c. *Cross-shore energy flux*

In this study, we focus on the cross-shore energy flux term, which estimates how much baroclinic tide energy propagates offshore into the deep ocean. The cross-shore energy flux in units of watts per square meter, which we will denote as $\mathcal{F}_{up}$ (u is the cross-shore velocity in our coordinate system) throughout the paper, is defined as

$$\mathcal{F}_{up}(x, z) = |u'(x, z)p'(x, z)| = \frac{1}{2}(u'_{\rm Re}p'_{\rm Re} + u'_{\rm Im}p'_{\rm Im}), \tag{24}$$

where $(\cdot)_{\rm Re}$ and $(\cdot)_{\rm Im}$ indicate the real and imaginary components, respectively, as both u' and p' are complex. Furthermore, we are interested in the vertically integrated cross-shore energy flux in watts per meter, defined as

$$\langle\mathcal{F}_{up}\rangle(x) = \int_h^0 \mathcal{F}_{up}(x, z)dz. \tag{25}$$

Throughout text, we will denote vertical integrals with $\langle\cdot\rangle$.

Because the boundary conditions impose that the solution is an internal inertia–gravity wave at the offshore boundary,

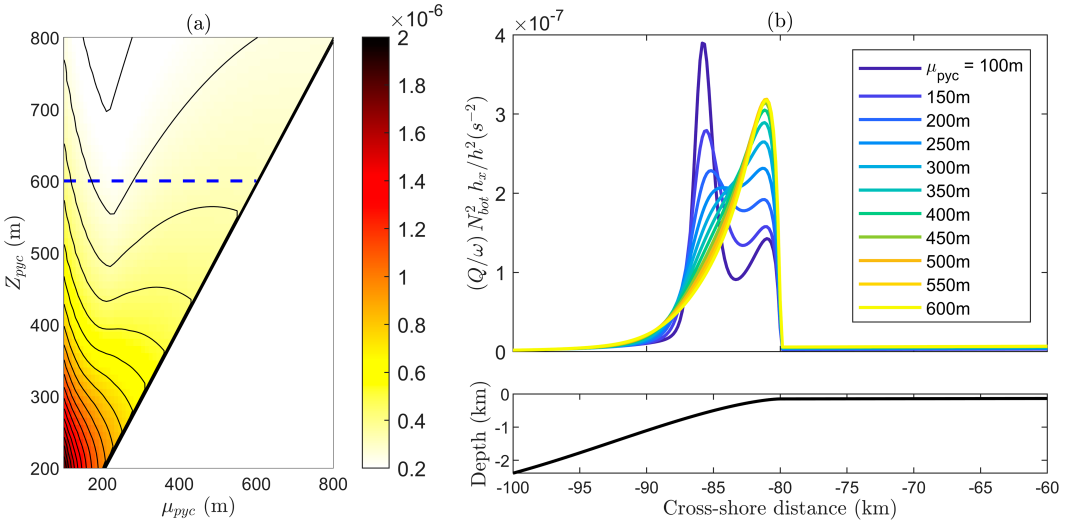

FIG. 4. (a) Maximum value of the Baines forcing $\tilde{F}_B$ in contour lines and color overlay; the dashed blue line is $Z_{\text{pyc}} = 600$ m. (b) Values of hydrostatic forcing $\tilde{F}_B$ from Eq. (23) as a function of cross-shore distance computed along the bottom for pycnocline depth 600 m [see dashed blue line in (a)] for different pycnocline thicknesses, zoomed in on the slope and shelfbreak region, where forcing is the largest. Shelf break is at $x = -80$ km as shown in the bathymetry profile in the bottom.

the pressure in each vertical mode can be used to determine the horizontal velocity via the u'–p' polarization relation from Eq. (12):

$$u'_j = \frac{\omega k_j}{\omega^2 - f^2} p'_j. \tag{26}$$

Notably,

$$C_j = -\frac{\omega^2 - f^2}{\omega k_j} \tag{27}$$

is the group velocity of the jth vertical mode. Then, the cross-shore energy flux at the offshore boundary is

$$\mathcal{F}_{up}|_{x=-L_x} = \left\langle \sum_{m=1}^{\infty} \sum_{n=1}^{\infty} \frac{\omega k_m}{\omega^2 - f^2} a_m a_n p'_m(z) p'_n(z) \right\rangle, \tag{28}$$

where a_m and a_n are the amplitudes of the mth and nth pressure modes. For normal modes, $\langle p'_m(z) p'_n(z) \rangle = 0$ for $m \neq n$, so

$$\mathcal{F}_{up}|_{x=-L_x} = \left\langle \sum_{m=1}^{\infty} \frac{\omega k_m}{\omega^2 - f^2} a_m^2 p'_m(z) p'_m(z) \right\rangle, \tag{29}$$

meaning that there is no contribution to the cross-shore energy flux from the cross terms, i.e., $\langle u'_m p'_n \rangle = 0$ for $m \neq n$.

3. Numerical solution approach

a. Numerical method

We implement the numerical method derived by Lindzen and Kuo (1969) to solve the coupled u'–p' equations [Eqs. (12) and (13)]. This method has been successfully implemented to solve both elliptic (subinertial) and hyperbolic (superinertial) differential equations in many previous studies (e.g., Chuang and Wang 1981; Sherwin and Taylor 1990; Dale and Sherwin 1996; Dale et al. 2001; Klymak et al. 2016). In this method, we write each of the coupled equations as

$$\mathbf{A}_{ix}\mathbf{R}_{ix-1} + \mathbf{B}_{ix}\mathbf{R}_{ix} + \mathbf{C}_{ix}\mathbf{R}_{ix+1} = \mathbf{D}_{ix}, \tag{30}$$

where $ix = 1{:}N_x$ is the horizontal index (N_x is the number of grid points in x and taken to be an even number); $\mathbf{R}$ is the vertical vector of length N_z (number of vertical grid points) of u' or p' at ix position; $\mathbf{A}_{ix}$, $\mathbf{B}_{ix}$, and $\mathbf{C}_{ix}$ are the operation matrices of size $N_z \times N_z$; and $\mathbf{D}_{ix}$ is the forcing vector of length N_z.

We use a staggered u'–p' grid in the horizontal direction, such that Eq. (12) is discretized and solved on the even grid points in x, and correspondingly, $\mathbf{R}_{ix}$ is $u'$and $\mathbf{R}_{ix-1}$ and $\mathbf{R}_{ix+1}$ are p'. Similarly, a discretized form of Eq. (13) is solved on the odd grid points in x, and correspondingly, $\mathbf{R}_{ix}$ is $p'$and $\mathbf{R}_{ix-1}$ and $\mathbf{R}_{ix+1}$ are u'. We solve the coupled u'–p' system of first-order equations rather than a single second-order equation for p' as in previous studies (e.g., Dale and Sherwin 1996; Zhang and Yankovsky 2016; Klymak et al. 2016). This two-equation formulation avoids a spurious mode that arises at $\omega = f$. At this tidal frequency, the relationship between u' and p' is singular [cf. Eq. (12)], which introduces problems with the boundary conditions for the second-order p' equation formulation. This spurious mode is avoided when the equations and the boundary conditions are recast in terms of both u' and p' (Dale et al. 2001).

Introducing matrices $\boldsymbol{\alpha}_{ix}$ and vectors $\boldsymbol{\beta}_{ix}$, we can pose the following recursive relation:

$$\mathbf{R}_{ix} = \boldsymbol{\alpha}_{ix}\mathbf{R}_{ix+1} + \boldsymbol{\beta}_{ix}. \tag{31}$$

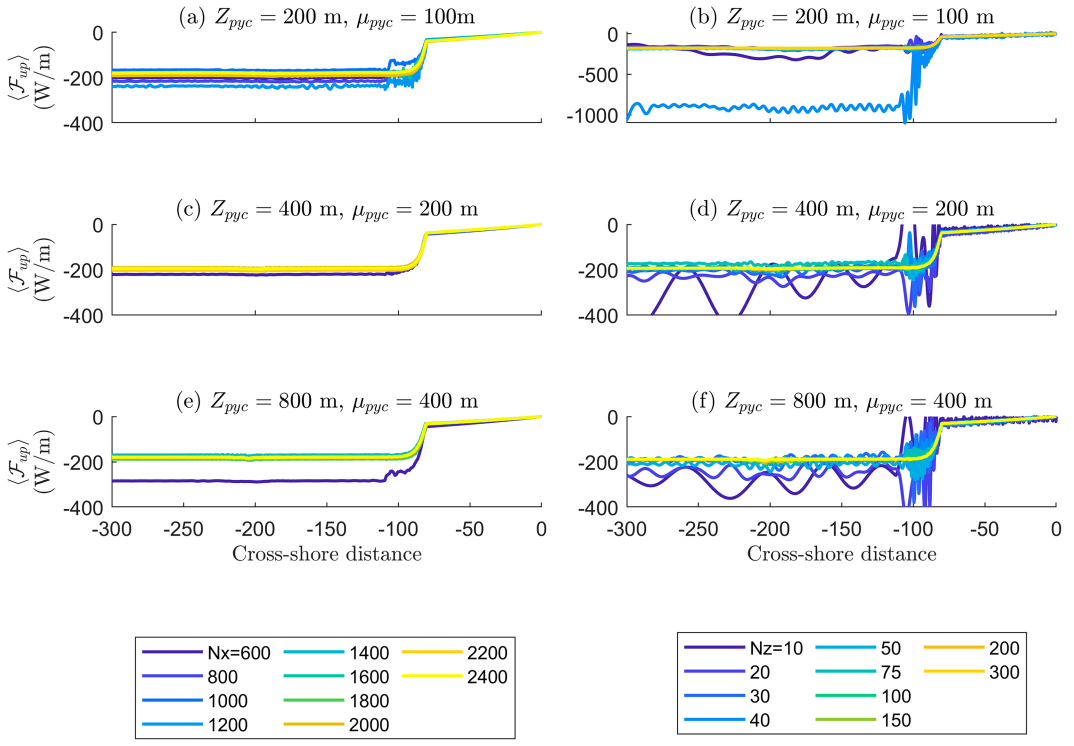

FIG. 5. Cross-shore energy flux $\langle \mathcal{F}_{up} \rangle$ computed for (a),(c),(e) different horizontal resolutions keeping $N_z = 300$ and (b),(d),(f) different vertical resolutions keeping $N_x = 1800$ for a selected sample of pycnocline depths and thicknesses. All values are computed for simulations forced with M_2 tidal forcing and with rigid-lid top boundary.

Plugging in Eq. (31) into Eq. (30), the recursive relations for $\boldsymbol{\alpha}_{ix}$ and $\boldsymbol{\beta}_{ix}$ are

$$\boldsymbol{\alpha}_{ix} = -\mathbf{C}_{ix}(\mathbf{A}_{ix}\boldsymbol{\alpha}_{ix-1} + \mathbf{B}_{ix})^{-1}, \tag{32}$$

$$\boldsymbol{\beta}_{ix} = (\mathbf{D}_{ix} - \mathbf{A}_{ix}\boldsymbol{\beta}_{ix-1})(\mathbf{A}_{ix}\boldsymbol{\alpha}_{ix-1} + \mathbf{B}_{ix})^{-1}. \tag{33}$$

From the vertical modes found using the offshore boundary condition solving Eq. (19), we can find $\boldsymbol{\alpha}_1$ and $\boldsymbol{\beta}_1$ at the open boundary and then find the remaining $\boldsymbol{\alpha}_{ix}$ and $\boldsymbol{\beta}_{ix}$ iterating forward using Eqs. (32) and (33). Finally, using the coastal boundary condition given by Eq. (14), we can solve for all $\mathbf{R}_{ix}$ iterating backward using Eq. (31).

b. Grid resolution dependence

All equations are solved on a Σ-grid, such that $\Sigma = z/h$ and $X = x$, and the derivatives are

$$\frac{\partial}{\partial X} = \frac{\partial}{\partial x} + \frac{z}{h}\frac{\partial h}{\partial x}\frac{\partial}{\partial z}, \qquad \frac{\partial}{\partial \Sigma} = h\frac{\partial}{\partial z}. \tag{34}$$

The domain is discretized with $N_x = 3800$ and $N_z = 300$ points in the horizontal and vertical directions, respectively, such that $\Delta x = 79$ m and $\Delta z = h\Delta\Sigma = (h/300)$ m, which in the deepest region is 10.3 m.

The resolution used in this study was chosen after performing sensitivity tests both to horizontal and vertical grid spacing to ensure that the solution has converged across the parameter space considered. Figure 5 shows cross-shore energy fluxes $\langle \mathcal{F}_{up} \rangle$ for several representative combinations of pycnocline depths and thicknesses computed in simulations. For these cases, we observe eventual convergence as we increase the horizontal (Figs. 5a,c,e) and vertical (Figs. 5b,d,f) resolutions.

Sufficiently high resolution is required to numerically solve this problem, in particular the eigenvalue problem at the offshore boundary shown in Eq. (19), which can be recast in the matrix form as

$$\mathbf{LV} = \mathbf{\Lambda M V}, \tag{35}$$

where $\mathbf{\Lambda}$ and $\mathbf{V}$ are, respectively, the eigenvalue and eigenvector matrices. Although we are solving the Sturm–Liouville eigenvalue problem that theoretically guarantees orthogonal eigenvectors, the vertically nonuniform stratification [second left-hand side term in Eq. (19)] makes the problem formulation nonselfadjoint (Carasso 1969). The finite-difference matrix on the left-hand side is nonsymmetric because of the first-order vertical derivative, and orthogonal eigenvectors are no longer guaranteed. In other words, while orthogonal eigenvectors are guaranteed in the case of a continuous differential equation problem of this type, they are not guaranteed in the discretized representation of this particular differential equation problem. For uniform stratification, matrix $\mathbf{L}$ is symmetric (second-order finite-difference matrix), so eigenvectors are guaranteed to be orthogonal.

As shown by Carasso (1969) and Gekeler (1974), for sufficiently small grid spacing Δz, one can construct a diagonal

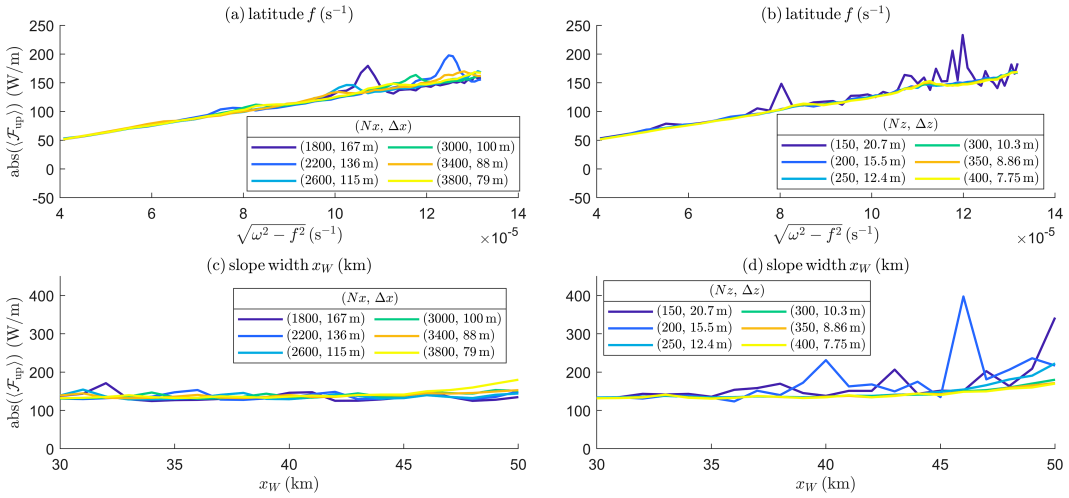

FIG. 6. Cross-shore energy flux $\langle\mathcal{F}_{up}\rangle$ computed for (a),(c) different horizontal resolutions given as the number of grid points N_x and horizontal spacing Δx ($N_z = 300$) and (b),(d) different vertical resolutions given as the number of grid points N_z and vertical spacing Δz ($N_x = 3800$) for the uniform stratification case. In (a) and (b), energy flux values are computed as a function of Coriolis parameter f, and in (c) and (d), values are computed as a function of slope width x_W. All values are computed for simulations forced with M_2 tidal forcing and with a rigid-lid top boundary.

matrix $\mathbf{D}$, such that $\hat{\mathbf{L}} = \mathbf{D}^{-1}\mathbf{L}\mathbf{D}$ is symmetric. The accuracy of computed eigenvalues increases with numerical resolution (Gheorghiu and Zinsou 2019; Early et al. 2020), which is necessary to accurately compute the associated eigenvectors. As such, the departure from orthogonality of the eigenvectors decreases with increased grid resolution. Furthermore, on a regularly spaced grid, in the case of nonuniform stratification, the grid points might not align with the Gaussian quadrature points (roots) of higher modes (eigenvector solutions), which requires increasing vertical resolution to resolve these modes, even if we can recast Eq. (19) in a self-adjoint form (Early et al. 2020). We find that for the resolution that we have chosen in this study ($N_z = 300$), the contribution to the computed cross-shore energy flux values from the cross-term components, which suggests nonorthogonal eigenvectors, is small (<5%).

Furthermore, horizontal resolution is also important because of the Σ-grid coordinates. In regions of steep topography, significant numerical errors may arise in computing the horizontal pressure gradient (Manabe and Smagorinsky 1967; Haney 1991). In models, the magnitude of the errors depends on the topographic gradient and strength of stratification, i.e., on how much the vertical isosurface coordinate is not aligned with the geopotential or isopycnal surfaces (Haidvogel et al. 2000; Sikirić et al. 2009). To address this problem in meteorological and oceanographic modeling, the following criterion known as the hydrostatic consistency was derived (Mesinger 1982; Haney 1991):

$$r = \left| \frac{\Sigma L_x (\partial h/\partial x)}{H} \frac{N_z}{N_x} \right| \leq 1. \tag{36}$$

However, it has been shown that in models, for instance ROMS, instability does not immediately occur for $r > 1$, and a grid can be numerically stable even for up to $r < 6$ (Shchepetkin and McWilliams 2003; Sikirić et al. 2009).

Here, we find that if the horizontal resolution is insufficient, the model yields resonance-like peaks for certain parameter values, even in the case of uniform stratification. That is, overall, we find that grid spacing with $N_x \sim 1800$ is sufficient for most parameter combinations, as shown in Figs. 5a, 5c, and 5e. However, as shown in Fig. 6, sweeping over values of Coriolis parameter f or slope width x_W, this horizontal resolution ($N_x = 1800$) produces peaks at certain values of f or x_W. Upon further inspection, energy flux beams generated in those simulations appear unphysical and indeed disappear as we increase N_x. Hence, we set $N_x = 3800$ in our simulations, which also meets the condition of $r < 6$ over the slope region. This resolution is equivalent to $\Delta x = 79$ m, which is much smaller than the $O(1)$ km spacing used in previous studies using Σ-coordinates (e.g., Sherwin and Taylor 1990; Dale et al. 2001; Klymak et al. 2016). Although the coarser resolution may have been sufficient for the coastal trapped waves of interest in these previous studies, we find that it is not sufficient for estimating the offshore baroclinic energy flux, which is the aim of this paper.

4. Model validation

We compare the output from our model with two other linear internal tide models: Coupling Equations for Linear Tides (CELT) (Kelly et al. 2013) and Centre de Météorologie Spatiale (CMS) (Papoutsellis et al. 2023). Numerical codes for both are publicly available and can be modified to match our topography setup in Fig. 1. Because the CMS model is currently restricted to uniform stratification, we take $N^2 = N_{bg}^2$ in all cases. We take the coastal shelf to be flat, i.e., $h_s = h_c$. The CELT model solves for vertical modes at each depth as if it is locally flat and then uses pressure and velocity matching conditions to adjust for changes in topography. These matching conditions allow for coupling of the modes. The CMS model uses

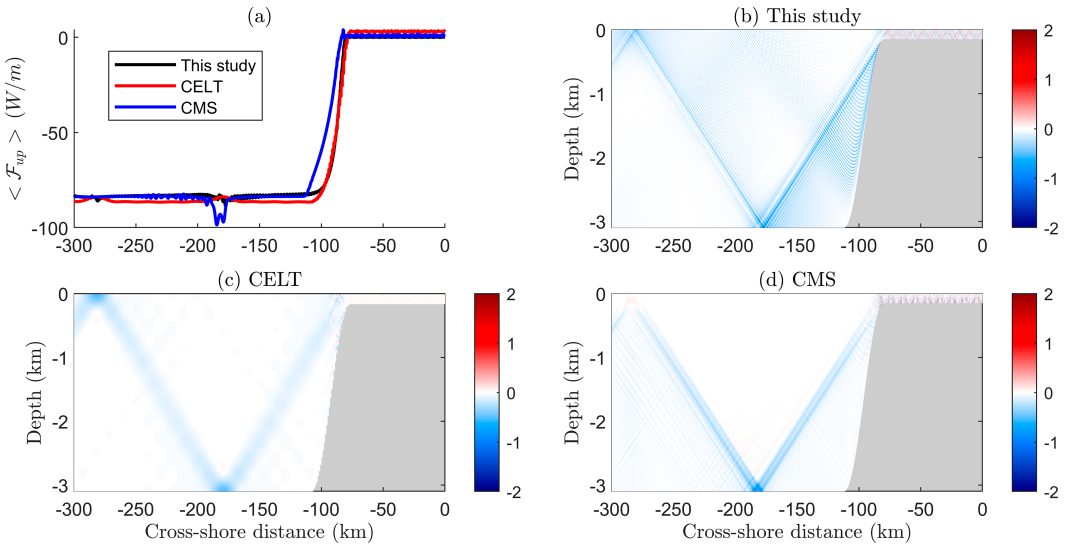

FIG. 7. Comparison of the linear internal tide model used in this study with CELT (Kelly et al. 2013) and CMS (Papoutsellis et al. 2023) for the uniform stratification case: (a) vertically integrated cross-shore energy flux $\langle \mathcal{F}_{up} \rangle$ computed using three different models; (b)–(d) spatial distribution of cross-shore energy flux $\mathcal{F}_{up}$ for the three different models.

local eigenfunction expansion of the streamfunction, which is advantageous because it satisfies the bottom boundary condition for any arbitrary topography. It then poses the problem in terms of a coupled-mode system of equations and solves them numerically.

One of the main differences between our model and these two models is in the definition of barotropic flux Q in the forcing term. Both the CELT and CMS define it in terms of the barotropic velocity u_{bt} and depth offshore, i.e., $Q = h_0 u_{\mathrm{bt}}(x = -L)$. Because the barotropic flow is assumed to be constant with the cross-shore distance, in 2D flows, barotropic velocity increases going toward the shore over the sloping region as the depth decreases. In Baines (1982), which we follow in our model, Q is approximated as the barotropic flux onto the shelf, i.e., shelf water "volume" ηx_s per tidal period $1/\omega$. The barotropic velocity at the shelf break is then implicitly prescribed as $u_{\mathrm{bt}}(x = -x_s) = Q/h_s = \eta x_s \omega / h_s$. What is the most appropriate model for barotropic currents in shallow regions is still uncertain (Zaron and Elipot 2021; Stammer et al. 2014) and beyond the scope of our process study. To be consistent in our comparison of the three models, we use $u_{\mathrm{bt}}(x = -x_s) = \eta x_s \omega / h_s = 0.75$ cm s^{-1} and find the appropriate offshore barotropic forcing that yields the same u_{bt} at the shelf break in the other two models. For $h_0 = 3100$ m, we need to set $Q = 6.5$ m^2 s^{-1} or equivalently $u_{\mathrm{bt}}(x = -L) = 0.21$ cm s^{-1} for the CELT and CMS runs.

We find that the spatial distribution and baroclinic energy flux magnitude for this test setup computed using our model match the outputs of the other two linear models (Fig. 7). The CELT model has vertically uniform grid spacing Δz throughout the domain, meaning that in order to have $\Delta z = 0.5$ m as we set over the shelf, quite fine vertical resolution of $Nz = 6200$ is required, and inverting such large matrices is computationally expensive. In our code, this problem is circumvented by using Σ coordinates. To be consistent with the number of vertical modes fully resolved at the offshore boundary in our model, we set $Nz = 300$, which corresponds to 12 resolved modes. As the model output was shown to be insensitive to the number of horizontal steps, especially for supercritical topography, in Kelly et al. (2013), we use 32 steps. The CMS model is more memory-intensive compared with our model and CELT, so we use 128 internal wave modes, which was the number suggested in Papoutsellis et al. (2023) to achieve convergence. The horizontal spacing is the same ($Nx = 3800$) as in our model.

Although idealized, our model presented here offers more flexibility to approximate the real ocean conditions in comparison with the other two linear tidal models. First, unlike our model, the CMS and other similar models (Griffiths and Grimshaw 2007; Lahaye and Llewellyn Smith 2020) are currently limited to uniform stratification. Second, both CELT and CMS assume radiating boundary condition, i.e., energy leaving the domain, along both horizontal boundaries at $x = 0$ and $x = -L$, unlike our model that imposes a coastal wall with $u = 0$ at $x = 0$. This is not a significant problem for supercritical topographies studied here, as internal tide propagation onto the shelf is small, though notably that results in small, but nonzero baroclinic energy flux on the shelf and at the coastal wall in those two models (Fig. 7a). However, for subcritical topographies, a significant portion of the waves can be reflected onto the shelf. The radiation boundary, which would allow this energy to leave the domain, might not be an appropriate choice at the coast, in contrast with a reflective wall boundary. However, it could also be argued that the radiation boundary can represent dissipation on the shelf in turbulent shallow water, which would prevent significant reflection.

5. Results

In this study, we are interested in the energy generated by the interaction of the gravest (barotropic Kelvin wave–like)

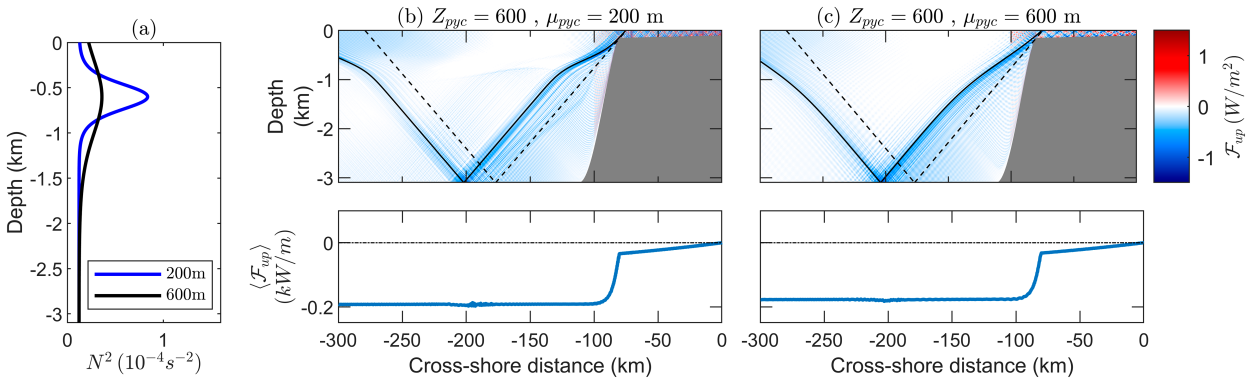

FIG. 8. Cross-shore energy flux (spatial structure and vertically integrated values) for (b) $Z_{\rm pyc} = 600$ m, $\mu_{\rm pyc} = 200$ m and (c) $Z_{\rm pyc} = 600$ m, $\mu_{\rm pyc} = 600$ m. The corresponding pycnoclines are shown in (a). All simulations are forced with M_2 tide and run with a rigid-lid boundary condition. Black dashed lines in (b) and (c) are the internal tide characteristics for uniform stratification case with slope $\sqrt{(\omega^2 - f^2)/(N_{\rm bg}^2 - \omega^2)}$, and black solid lines are the characteristics for the specific nonuniform stratification profiles with slope $\sqrt{(\omega^2 - f^2)/(N^2 - \omega^2)}$.

mode with the coastal topography. The gravest mode for all configurations is at $l = 0$ (not shown). This is the case for the rigid-lid boundary condition, and when we impose a free-surface boundary condition, in general, $l \neq 0$ for the gravest mode (not shown). However, the rigid-lid boundary condition and the corresponding zero alongshore variability are consistent with the assumptions made in Baines (1982) to derive the barotropic tide body force that we use in this study.

In this section, we will investigate the sensitivity of cross-shore energy flux to the nonuniform stratification, in particular pycnocline depth $Z_{\rm pyc}$ and thickness $\mu_{\rm pyc}$. In our setup, all of the nonuniform stratification profiles have approximately the same depth-averaged N^2 (denoted as $\overline{N^2}$) at the offshore boundary, which is approximately $1.75N_{\rm bg}^2$. We will also assess how the presence of a pycnocline affects the cross-shore energy flux by comparing the simulations with nonuniform stratification to those with uniform stratification with $N^2 = N_{\rm bg}^2$ and $N^2 = \overline{N^2} = 1.75N_{\rm bg}^2$. It is important to recall that in our setup, energy flux is directed westward (negative x direction), and hence, $\langle \mathcal{F}_{up} \rangle_{x=-Lx}$ is negative; therefore, in the parameter sweeps, we plot its absolute value, and terms such as "increase" and "decrease" refer to the magnitude of the flux.

a. Cross-shore energy flux

Figure 8 shows cross-shore energy flux $\mathcal{F}_{up}(x, z)$ and vertically integrated values $\langle \mathcal{F}_{up} \rangle(x)$, defined in Eqs. (24) and (25), respectively, for M_2 tidal forcing runs for pycnocline depth of 600 m. The middle panel (Fig. 8b) shows the energy flux for simulations with the relatively narrower pycnocline $\mu_{\rm pyc} = 200$ m, corresponding to the blue line in the stratification profiles, and the right panel (Fig. 8c) one with relatively thicker pycnoclines ($Z_{\rm pyc} = \mu_{\rm pyc}$), corresponding to the black stratification profile lines. We find beam-like structure of the energy flux with bottom and surface reflections, as has been previously predicted by theory (Craig 1987) and observed in numerical simulations (Kelly et al. 2010). Overall, we find that the magnitude of the cross-shore flux does not vary significantly with stratification, so we only show representative results in Fig. 8. However, the pycnocline depth and thickness changes the spatial distribution of the energy flux. For instance, there is elevated near-surface energy flux magnitude and the beam is distorted for simulations with narrower pycnoclines compared with the thicker pycnoclines that approach uniform stratification. The effect of the pycnocline can also be seen from the deviation of the tidal beams (characteristics in solid black lines) from the black dashed lines, which are internal tide characteristics assuming constant background stratification. The specifics of the sensitivity to pycnocline depth and thickness and the interplay between stratification and topography will be discussed in detail in sections 5b–5d.

b. Examining previously derived scalings

We find the same latitudinal dependence of the cross-shore energy flux magnitude as previously derived for knife-edge ridge (Llewellyn Smith and Young 2003) and topographic step (St. Laurent et al. 2003), i.e., $\langle \mathcal{F}_{up} \rangle_{x=-Lx} \propto \sqrt{\omega^2 - f^2}$ (cf. Fig. 9a). This is, of course, because the group speed nonlinearly decreases with latitude, that is, the eigenvalues at the offshore boundary defined in Eq. (19) $k_j \propto \sqrt{\omega^2 - f^2}$, and it can be inferred from Eq. (27) that $C_j \propto \sqrt{\omega^2 - f^2}$ for a given forcing frequency ω, which translates to the decrease of cross-shore energy flux with latitude.

Varying the shelf width x_s, we find that $\langle \mathcal{F}_{up} \rangle \propto x_s^2$ (Fig. 9b). This relationship is perhaps not surprising as the magnitude of the forcing $\tilde{F}_B$ is linearly dependent on x_s. Furthermore, this is consistent with the previously derived scaling of the energy flux magnitude being proportional to the square of barotropic velocity. The barotropic velocity at the shelf break is defined as $u_{\rm bt} = Q/h_s = \omega x_s \eta / h_s$; therefore, $\langle \mathcal{F}_{up} \rangle_{x=-Lx} \propto u_{\rm bt}^2 \propto x_s^2$ for a fixed tidal frequency ω and barotropic tidal elevation at the coast η.

c. Sensitivity of cross-shore energy flux to stratification and topography

As the topographic criticality $\alpha_{\rm max}$ depends on both stratification and topographic slope [cf. Eq. (1)], we now investigate the effects of the interplay between the stratification and

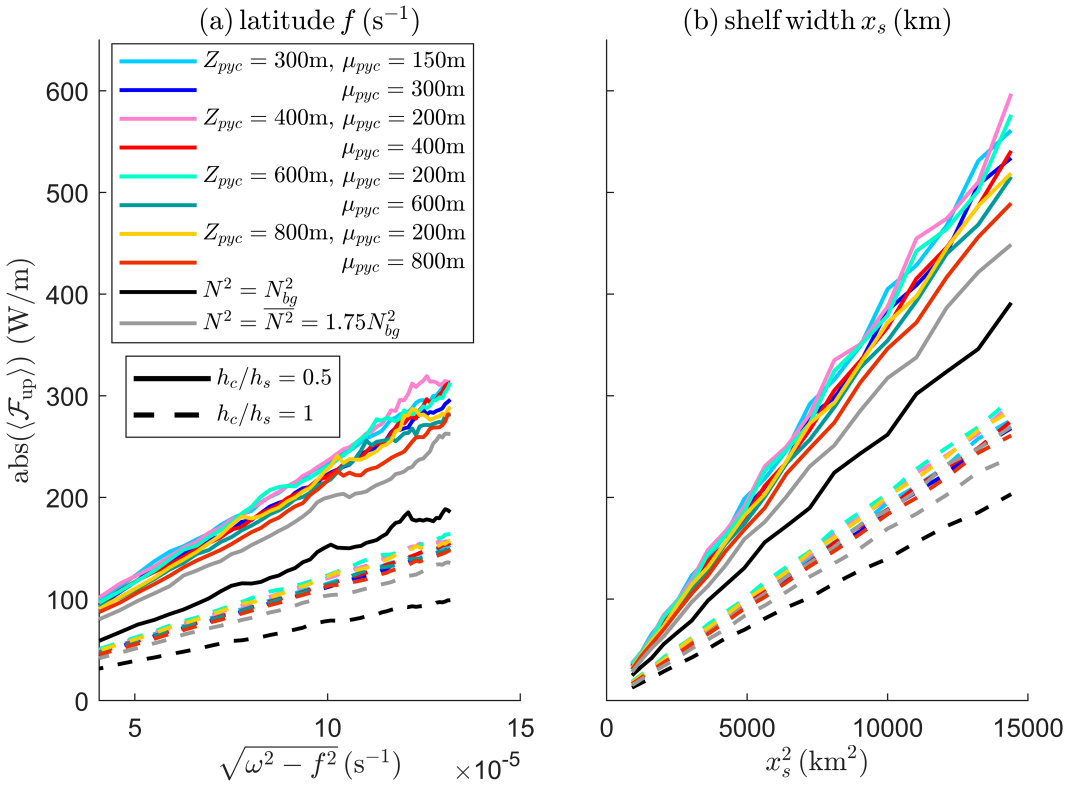

FIG. 9. Cross-shore energy flux $\langle \mathcal{F}_{up} \rangle$ at the offshore boundary $x = -L_x$ as a function of latitude in terms of (a) $\sqrt{\omega^2 - f^2}$ and (b) x_s^2. Energy flux is computed for nonuniform stratification profiles' varying pycnocline depth Z_{pyc} and thickness μ_{pyc} and also for uniform stratifications $N^2 = N^2_{\text{bg}} = 1.22 \times 10^{-5}\,\text{s}^{-2}$ (black line) and $N^2 = 1.75N^2_{\text{bg}} = 2.14 \times 10^{-5}\,\text{s}^{-2}$ (gray line).

topography on the cross-shore energy flux. Specifically, in Eq. (3), we vary (i) the width of the slope x_W between 30 and 60 km ($x_W = 32$ km in the main setup), (ii) the depth of the shelf h_s between 150 and 600 m ($h_s = 150$ km in the main setup), and (iii) the ratio of the coastal depth to shelf depth h_c/h_s over the range 0.5–1 ($h_c/h_s = 2/3$ in the main setup), while keeping all of the other simulation parameters the same and fixing $f = 0.93 \times 10^{-4}\ \text{s}^{-1}$ (~40°). The last parameter h_c/h_s does not affect the topographic criticality α_{max} of the slope. In all cases considered here, $\alpha_{\text{max}} > 1$, i.e., the topography is supercritical, with respect to M_2 tide characteristics. We present these results to show some of the effects of different topographies and show results with smaller α_{max} values (i.e., more gradual slopes) comparable with some previous studies (Craig 1987; Kelly and Nash 2010; Hall et al. 2013; Wang et al. 2018).

Overall, at a fixed latitude, the energy flux is smaller for deeper shelves as shown for a sample stratification profile with pycnocline depth of 600 m and thickness of 200 m in Fig. 10a. Varying the pycnocline depth and thickness, the energy flux values predominantly collapse onto one curve, such that $\langle \mathcal{F}_{up} \rangle \propto 1/h_s$ (Fig. 10b). For smaller h_s, there is about 10% variability depending on the stratification. In the expression for cross-shore energy flux derived by Baines (1982), $\langle \mathcal{F}_{up} \rangle$ increases with Z_{pyc}/h_s, which is consistent with our finding here, although we do not find strong dependence on Z_{pyc}. The expression in Baines (1982) is only valid for $Z_{\text{pyc}}/h_s \leq 1$, i.e., pycnoclines that are shallower than the shelf break. Here, we extend the analysis to $Z_{\text{pyc}}/h_s > 1$, i.e., deeper pycnoclines, and show that similarly $\langle \mathcal{F}_{up} \rangle \propto 1/h_s$.

In general, as we vary h_s, the magnitude of the energy flux increases with the topographic criticality parameter α_{max} (Fig. 10c), though the rate of change of $\langle \mathcal{F}_{up} \rangle$ with α_{max} is dependent on the stratification profile. The increase in energy flux here appears to be exponential with α_{max}, not linear as was previously estimated by Craig (1987). However, we consider the values of α_{max} even larger than those in Craig (1987), and for the smaller α_{max} values in our range, the relationship could be approximated as linear.

The energy flux is also smaller for flatter shelves (i.e., larger h_c/h_s) as shown in Fig. 10a. As the value of coast depth h_c is doubled, $\langle \mathcal{F}_{up} \rangle$ is approximately reduced by a factor of two (cf. solid and dashed lines in Fig. 10b). Figure 10c also highlights that the slope of the shelf itself (i.e., h_c/h_s) is an important parameter. Varying h_c/h_s does not change α_{max}, but it does change the energy flux. However, the effect of this parameter is not thoroughly studied, as most works on the sensitivity of energy flux to topography are focused on the effects of α_{max}.

Over our selected range of slope widths x_W, the magnitude of the cross-shore energy flux does not vary, even though α_{max} varies with x_W (Figs. 10d,e). In Baines (1982) formulation, the parameter

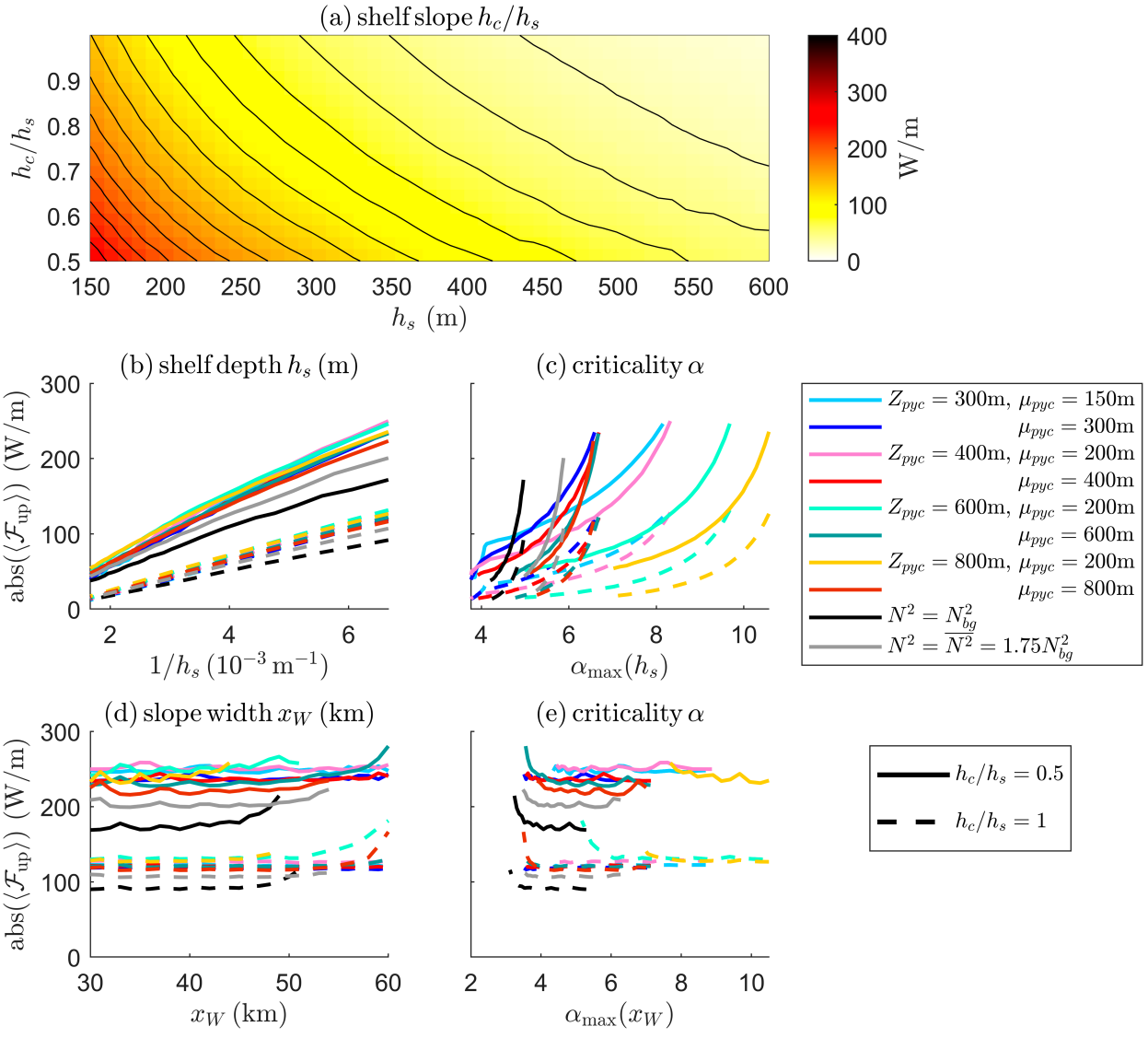

FIG. 10. (a) Cross-shore energy flux $\langle \mathcal{F}_{up} \rangle$ at the offshore boundary as a function of shelf depth h_s and the ratio of coastal depth to shelf depth h_c/h_s for $Z_{pyc} = 600$ m, $\mu_{pyc} = 200$ m; $\langle \mathcal{F}_{up} \rangle$ at the offshore boundary for several selected stratification profiles as (b) a function of $1/h_s$, (c) a function of $\alpha_{max}(h_s)$, (d) a function of x_W, and (e) a function of $\alpha_{max}(x_W)$. In (b)–(e), solid lines are for $h_c/h_s = 0.5$ and dashed lines are for $h_c/h_s = 1$. All values are computed for a fixed $f = 0.93 \times 10^{-4}$ s^{-1} (~40°).

x_W does not explicitly appear but contributes by changing the slope h_x through the parameter $T = (h_s\sqrt{\omega^2 - f^2})/(h_x\sqrt{g' Z_{pyc}})$, where $g' = g\Delta\rho/\rho_0$. However, for our chosen parameter range, T only varies between 0.3 and 0.9, which would have an insignificant effect on the expression in Baines (1982), consistent with our result of energy flux magnitude not depending on x_W. This can also be explained by the fact that most of the forcing $\tilde{F}_B$ occurs at or close to the shelf break (cf. Figs. 3 and 4b) for our chosen ranges of Z_{pyc} and μ_{pyc}. As such, the maximum value and area integral of the forcing function are mostly not sensitive to the width of the slope x_W, as we will see in section 5d and the appendix, thus not affecting the magnitude of the baroclinic energy flux. Gerkema et al. (2004) similarly found that the magnitude of barotropic-to-baroclinic energy conversion does not depend on the slope width. Notably, we find that for deeper pycnoclines and a uniform stratification profile, simulation results with wider x_W are sensitive to resolution and, for our chosen resolution, begin to drift due to unphysical numerical errors at larger x_W. Hence, we omit those values in Figs. 10d and 10e.

We also find that the energy flux for nonuniform stratification profiles (colored lines in Figs. 9 and 10) is greater than that for the uniform stratification profiles (black and gray lines in Figs. 9 and 10). This is in part because the nonuniform stratification profiles have a peak that is larger than N^2_{bg}; hence, the forcing term is also larger [cf. Eq. (23)]. However, for nonuniform stratifications, the maximum value of N^2 is also not the determining factor, as it can vary by at least a factor

of three depending on the pycnocline thickness (cf. Fig. 1c), yet the energy flux magnitude only varies by about 10% over the range of pycnocline depths and thicknesses considered here. Therefore, the presence of a pycnocline itself, and not its particular shape, seems to result in larger baroclinic energy flux magnitude. Even the energy flux curves for stratification profiles with deeper and thicker pycnoclines, e.g., $Z_{\mathrm{pyc}} = \mu_{\mathrm{pyc}} = 600$ m and $Z_{\mathrm{pyc}} = \mu_{\mathrm{pyc}} = 800$ m, for which the stratification profile approaches that of a uniform stratification, collapse onto a similar line as the energy flux curves for shallower and narrower pycnoclines.

Notably, group speed does not depend on the pycnocline thickness; there is only a small change in k_j in Eq. (27) as we change Z_{pyc} and μ_{pyc} at a given latitude. However, k_j is larger in the case of uniform stratification compared with the nonuniform stratification profiles. That results in slower group velocity and smaller baroclinic energy flux magnitude for the uniform stratification case.

d. Scaling of cross-shore energy flux magnitude

In this section, we summarize the combined previously and newly found latitudinal and topographic effects on the cross-shore energy flux magnitude that we investigated separately in sections 5b and 5c, respectively. As we have shown in these previous sections, the topographic criticality parameter $\alpha_{\max}$ does not capture the variability in the magnitude of baroclinic energy flux well. As such, we seek to find a better scaling that explains the dependence of the energy flux magnitude on the parameters explored in this study.

We derive a scaling for the baroclinic energy flux magnitude, using the relationships found in sections 5b and 5c and the energetics arguments in Baines (1982), to be

$$\langle \mathcal{F}_{up} \rangle \propto \frac{\langle \tilde{F}_B \rangle_A}{\langle \tilde{F}_B \rangle_A^0} \frac{\eta x_s}{h_c} \sqrt{\omega^2 - f^2}. \tag{37}$$

Here, $\langle \tilde{F}_B \rangle_A$ is the area integral of the Baines body force function [i.e., Eq. (22)] that depends on x_s, h_s, h_c, η, and N^2; specifically, $\langle \tilde{F}_B \rangle_A \propto \eta x_s (h_c/h_s)$. The term $\langle \tilde{F}_B \rangle_A^0$ is the area integral of the Baines body force function for some baseline topographic parameters (x_s^0, h_s^0, h_c^0, η^0) for a particular stratification N^2. Here, for each (Z_{pyc}, μ_{pyc}), we compute $\langle \tilde{F}_B \rangle_A^0$ as the area integral of Eq. (22) setting $x_s^0 = 30$ km, $h_s^0 = h_c^0 = 150$ m, and $\eta^0 = 0.05$ m. In this manner, the first fraction of Eq. (37) normalizes for the N^2 dependence of $\tilde{F}_B$. Derivation details are summarized in the appendix.

Notably, the derivation of Baines body force in Eq. (21) assumes that the cross-shore barotropic velocity at the shelf break is $u_{\mathrm{bt}} = (Q/h_s)\exp(-i\omega t)$ (Baines 1973). Then, the expression in Eq. (37) for baroclinic energy flux can be rewritten as

$$\langle \mathcal{F}_{up} \rangle \propto \frac{u_{\mathrm{bt}}^2 h_s}{\langle \tilde{F}_B \rangle_A^0} \sqrt{\omega^2 - f^2}. \tag{38}$$

This expression shows that the scalings previously derived for the energy fluxes of baroclinic tides generated isolated ridge (Llewellyn Smith and Young 2003) and step topography (St. Laurent et al. 2003), namely, the dependence on $u_{\mathrm{bt}}^2\sqrt{\omega^2 - f^2}$, also hold for the generation in the presence of supercritical coastal topography despite the difference in geometry and imposed boundary conditions.

To test our scaling, we run full parameter sweeps for different stratifications (Z_{pyc} and μ_{pyc}) varying $f = 0.8 \times 10^{-4}$–1.35×10^{-4} s^{-1}, $x_s = 30$–120 km, $h_s = 150$–600 m, $h_c/h_s = 0.5$–1, and $\eta = 0.05$–0.2 m. Our results, summarized in Fig. 11, indicate that our scaling from Eq. (37) (Fig. 11a), which is derived using specific topographic parameters, approximates the baroclinic energy flux variability well. In contrast, the topographic criticality parameter $\alpha_{\max}$ (Fig. 11b), the expression which does not consider the topographic parameters in detail, is not a good scaling for the baroclinic flux magnitude.

The expression in Eq. (37) can be used at a given location in the ocean using data for local bathymetry and stratification. For instance, a piecewise fit in the form of Eqs. (2)–(4) to a realistic topographic profile can be calculated to find the relevant topographic parameters x_s, h_c, h_s, and h_0. Examples of such curve fits are shown in Fig. 2. The area integral of the Baines body force $\langle \tilde{F}_B \rangle_A$ can be found semianalytically by integrating Eq. (22). These values would be sufficient to approximate the magnitude of the offshore energy flux. The term that corrects for stratification $\langle \tilde{F}_B \rangle_A^0$ can be computed using our numerical model for any given stratification and bathymetry profile or approximated using the expression in Eq. (A6). However, we found this term to have less impact on the offshore energy flux magnitude compared with the other terms in Eq. (37), which suggests that the estimates of the topographic parameters and body force integral $\langle \tilde{F}_B \rangle_A$ are sufficient to approximate the magnitude of the offshore baroclinic energy flux relatively easily.

6. Discussion and conclusions

In this study, we conduct a series of idealized numerical simulations in order to investigate the sensitivity of the magnitude of the cross-shore energy flux generated by the interaction of barotropic semidiurnal tide with supercritical topography. The generation of baroclinic tides at the continental slope is a complicated problem, and it is difficult to exhaustively investigate the sensitivity of the radiated baroclinic energy flux, even though we already consider a wide range of parameters. However, the numerical framework developed in this study makes it easy to further explore the relevant parameter spaces.

Here, we specifically explore the dependence of the energy flux magnitude on 1) latitude, 2) topographic parameters, and 3) nonuniform stratification by varying pycnocline thickness and depth. The first two parameter categories were considered in the ray-tracing analysis by Baines (1982). Here, we extend that work to pycnoclines that are deeper than the shelf break and with thickness of the same order of magnitude as their depth. As such, the stratification profiles we consider are akin to deep and relatively thick permanent thermoclines often present in the ocean (Gerkema et al. 2004; Vieira and Allshouse 2020), in contrast with the shallow and infinitesimally thin pycnocline that resembles a seasonal (summer) pycnocline in the Baines (1982) model.

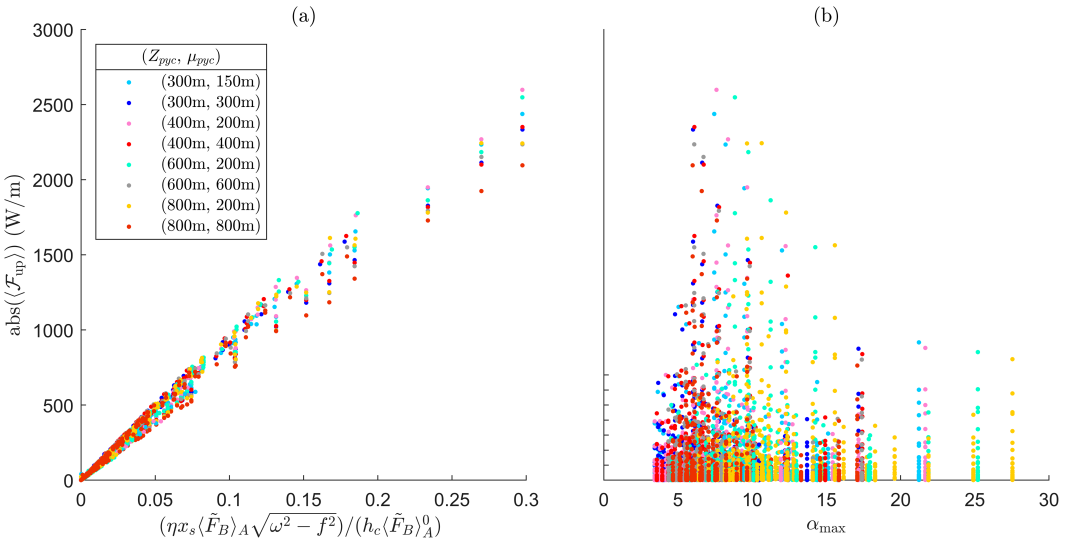

FIG. 11. The dependence of cross-shore energy flux $\langle \mathcal{F}_{up} \rangle$ at the offshore boundary for different stratifications on latitude and topographic parameters in Eqs. (2)–(4) as a function of (a) scaling parameter defined in Eq. (37) and (b) topographic criticality parameter α_{max} defined in Eq. (1).

We present the sensitivity of the cross-shore baroclinic tide energy flux in terms of both the physical parameters (e.g., latitude, shelf width, and pycnocline depth/thickness) and the nondimensional topographic criticality parameter α_{max} [cf. Eq. (1)], which is commonly used in studying the tide–topography interactions. We draw three main conclusions from our findings for the ranges of parameters considered here:

1) For the nonuniform stratification profiles, cross-shore energy flux magnitudes are more sensitive to the latitude and topographic parameters than to pycnocline depth and thickness; yet, the presence of a pycnocline amplifies the energy flux magnitude compared with uniform stratification cases, and the variability of energy flux magnitude cannot be simply explained by the values of deep-ocean N^2, depth-averaged N^2, or maximum N^2.
2) The magnitude of cross-shore energy flux is not simply governed by the topographic criticality: self-similar regimes appear in terms of physical parameters: specifically, the cross-shore energy flux decreases with latitude (f), increases with shelf width (x_s), decreases with shelf depth (h_s), and remains unchanged with slope width (x_W).
3) Cross-shore energy flux magnitude is sensitive to the slope of the coastal shelf itself, which has been previously neglected as the shelf is often modeled to be flat.

Our findings are of particular interest, as many previous studies were focused on the effects of topographic criticality α_{max} on the magnitude of the baroclinic energy flux (e.g., Craig 1987; Hall et al. 2013; Kelly 2016; Wang et al. 2018). However, we find α_{max} to be a poor nondimensional parameter to describe baroclinic tide generation at the coast. For example, the energy flux scales with $1/h_s$, i.e., it increases with shallower shelf break and steeper topographic slope, meaning that it increases with α_{max}. Yet, the energy flux magnitude remains relatively constant with the width of the slope x_W, even though narrower slope increases the value of α_{max}. Although pycnocline thickness and depth can change the value of α_{max}, the energy flux magnitude is not very sensitive to differences in stratification at a fixed latitude and for a given set of topographic parameters.

Instead, we find that the energy flux magnitude depends on many physical parameters that describe the system. Using scaling analysis and energetic arguments, we find a scaling parameter that captures the dependence of the baroclinic energy flux on topographic parameters, latitude, and stratification better than α_{max} does. Therefore, we propose that although α_{max} captures the transition of the topography from subcritical to supercritical regimes with respect to the baroclinic tide propagation, Eq. (37) provides a better scaling for the baroclinic energy flux magnitude itself. The sensitivity of the baroclinic energy flux to some of the topographic parameters that we find to be important has not been previously considered in the context of generation at continental slopes. For instance, Gerkema et al. (2004) found that the conversion rate at any supercritical slope can be closely approximated by the theoretical value derived for step topography in St. Laurent et al. (2003), but the only parameter varied was the slope width x_w, which we also find to have small impact on the baroclinic energy flux magnitude. However, we caution the reader that the new scaling derived here relies in part on particular assumptions made in Baines (1973) to estimate the cross-shore barotropic velocity, u_{bt}, dependence on which is evident in Eq. (38). As such, accurate estimates of the baroclinic energy flux rely on accurate estimates of barotropic currents. In future studies, it will be useful to compare the estimates of energy fluxes using measured tidal elevation and estimated tidal currents from satellite measurements, such as TOPEX/Poseidon (Egbert and Erofeeva 2002) or AVISO.

Interestingly, one of the parameters that significantly affects the baroclinic energy flux magnitude in our results is the slope of the continental shelf itself. We find that the energy magnitude inversely scales with a ratio of the water depth at the coast to the depth at the shelf break. Yet, to our knowledge, this parameter has not been studied, in part because it does not affect the topographic criticality α_{max}, and it does not appear in the analytical expression in Baines (1982), which assumes a flat continental shelf. In all of our simulations, the continental shelf remains subcritical ($\alpha \ll 1$) and has a significantly more gentle slope than the continental slope. Switching to CELT and CMS models with onshore radiation boundary condition, we find insignificant differences in the cross-shore energy flux between setup with flat and sloping continental shelf, so it is possible that the differences that we find in our study are largely due to the reflective wall boundary condition. A careful consideration of the appropriateness of each boundary condition is beyond the scope of this study; although wave energy dissipation due to breaking near the coast is better captured by the radiation boundary condition, an argument from observations of standing internal tides on continental shelves (Lerczak et al. 2003; Rayson et al. 2012; Suanda and Barth 2015) can also be made in favor of reflections from the coast. Regardless, many modeling studies choose to represent the coastal boundary as reflective, both in linear models (e.g., Dale et al. 2001; Zhang and Yankovsky 2016) and full-equation models (e.g., Hall et al. 2013; Klymak et al. 2016). Hence, it is important to document how the slope of the continental shelf affects the energy flux under the assumption of a coastal wall.

For our selected range of parameter values, energy flux magnitudes correlate with the areal integral rather than the maximum value of the forcing function. Furthermore, the location on the slope where the forcing function has the maximum value, which depends on the pycnocline thickness and depth, does not significantly affect the energy flux magnitude. However, it is possible that the specific functional approximation of the bathymetry used in this study [cf. Eqs. (2)–(4)] makes the shelf break a particularly important location for the generation of the internal tide beam (Chen et al. 2017). As such, the shape of the continental slope (e.g., piecewise linear as in this study, Gaussian, or sinusoidal) may be another parameter that needs to be considered, as was previously suggested by Wang et al. (2018) in the case of uniform stratification. That is, it is possible that pycnocline thickness and depth play a more important role if the bathymetry is smoother at the shelf break, which needs to be explored in a future study.

Although we see the imprint of the pycnocline depth and thickness in the spatial distribution of the cross-shore energy flux, most of the energy propagates offshore as a single beam in our simulations; mode 1 accounts for a large fraction in offshore energy flux. However, global maps of baroclinic tide energy reconstruction from climatology data by de Lavergne et al. (2019) suggested that modes 2–5 can be important in many coastal regions. Barbot et al. (2021) found that in the Bay of Biscay, the mode 1 baroclinic tides are controlled by maximum N around 750-m depth, akin to the deep permanent pycnoclines considered in this study. In contrast, modes 2 and 3 baroclinic tides are controlled by N at much shallower depths (~20–40 m), i.e., seasonal near-surface secondary pycnoclines. One of the interesting continuations of our study would be to add a shallow pycnocline to investigate its effect on the baroclinic energy flux magnitude and its modal decomposition, which is possible using our model, as stratification is expected to be responsible for setting the modal wavelengths (Llewellyn Smith and Young 2002). This would assess whether baroclinic energy flux might be seasonally variable, which may be especially important in temperate and subpolar regions, where seasonal differences in stratification are more significant, yet not captured in global estimates.

In this study, we consider a 2D linear model, the advantage of which is allowing us to perform sweeps over a wide range of parameters using a reasonable number of computational resources. Similar models have been used in a number of previous studies in unstratified and stratified systems (e.g., Sherwin and Taylor 1990; Dale and Sherwin 1996; Dale et al. 2001; Klymak et al. 2016; Yankovsky and Zhang 2017). Our examination of the numerical approach revealed that the finite-difference method used to solve this problem requires high spatial (vertical and horizontal) resolution, especially when stratification is nonuniform. The cross-shore energy flux may be under- or overestimated if the problem is underresolved and, furthermore, results in unphysical solutions that show up as resonance-like peaks in the parameter sweeps. The grid size that we find to be sufficient for the solution to converge ($\Delta x \lesssim 100$ m, $\Delta z \lesssim 100$ m in our setup) is much smaller than that used in some of the previous studies (e.g., Sherwin and Taylor 1990; Dale and Sherwin 1996; Dale et al. 2001; Klymak et al. 2016). Now that we have established a setup for this problem, we can use this tool to update the global estimate of the baroclinic internal tide energy flux, previously computed by Baines (1982), with more accurate approximations of coastal bathymetry and stratification.

However, the linear setup of simulations in this study limits the consideration of several aspects that may be important to the generation and propagation of the baroclinic tides. First, we are neglecting the alongshore variation; previously, Katsumata (2006) showed that 2D simulations may underestimate the offshore energy flux by up to an order of magnitude compared with 3D simulations. Alongshore variations in topography can also result in changes in propagation of the Kelvin wave–like barotropic mode itself (Yankovsky and Zhang 2017), which means that the assumptions made to derive Baines body forcing no longer hold. Furthermore, due to the complex nature of bottom topography, baroclinic wave beams that are prevalent in 2D simulations may be more scattered in a realistic 3D ocean (Lamb 2014). The rigid-lid boundary condition also leads to neglecting the alongshore variation, as the gravest mode has zero alongshore wavenumber. In contrast, with the free-surface boundary condition, the alongshore wavenumber of the gravest mode is nonzero. In this case, internal tides propagate at an oblique angle to the coast and "leaky" superinertial coastal trapped waves that redistribute energy are possible (Dale and Sherwin 1996; Musgrave 2019).

This setup also does not allow for nonlinear wave interactions, which might play an important role (Gerkema et al. 2006; Maugé and Gerkema 2008; Duda et al. 2012; Wang et al. 2021), in particular in transferring energy to higher frequencies and local dissipation (Grisouard and Staquet 2010; Gayen and Sarkar 2011a; MacKinnon et al. 2017). Increased shear from internal wave beams can also further enhance local dissipation and mixing (Fructus et al. 2009). The relative effects of these processes must

be considered in future studies with fully nonlinear 3D simulations. Nevertheless, because the problem of baroclinic tide energy at the coastal margins is dependent upon many factors (e.g., topographic slope, tidal forcing frequency, and stratification), this process study provides insights into the sensitivity of the energy flux magnitude and modal decomposition sweeping over a wide range of parameters.

Acknowledgments. This work was supported by the following NSF Grants: for JAL, OCE-1155799; for V. E. Z. and J. A. L., OCE-1756752 and OCE-2220439. R. C. M. acknowledges funding from the Canada Research Chairs Program. The authors thank three anonymous reviewers for their comments to help improve the manuscript.

Data availability statement. All MATLAB codes necessary to run a simulation for a given topography and stratification are provided in a GitHub repository (https://zenodo.org/record/8225828, https://doi.org/10.5281/zenodo.8225828). This repository also contains all the relevant data for a sample simulation and baroclinic energy flux data for the parameter sweeps performed in this study in MAT-file format, as well as scripts for visualizing these outputs in MATLAB and in Python.

APPENDIX

Derivation of the Baroclinic Energy Flux Scaling

Here, we derive a scaling for the cross-shore baroclinic energy flux magnitude. From the energetics arguments in Baines (1982) and our simulation results in sections 5b and 5c, we find that

$$\langle \mathcal{F}_{up} \rangle \propto \frac{\eta^2 x_s^2}{h_s} \sqrt{\omega^2 - f^2}. \tag{A1}$$

We further assume that the energy flux magnitude scales with the area integral of the Baines body force $\tilde{F}_B$. For the sake of simplicity, we will use the hydrostatic approximation of the forcing term given in Eq. (23) in the derivations here, though we use the full term given in Eq. (22) in our calculations.

From Fig. 3, we can approximate the area integral of $\tilde{F}_B$ as the sum of two trapezoids: 1) area A_1 on the continental shelf with height x_s and lengths of bases equal to h_c and h_s and 2) area A_2 on the continental slope with height x_s' and lengths of bases equal to h_s and h_s'. We denote x_s' to be the horizontal extent of the nonzero $\tilde{F}_B$ on the slope, and $h_s' = h(x_s')$. The approximate area integral denoted by $\langle \cdot \rangle_A$ is

$$\langle \tilde{F}_B \rangle_A = \int_A \frac{\eta x_s N^2 h_x}{h^2} dx dz, \tag{A2}$$

$$\sim \frac{\eta x_s}{h_s^2} \left(\frac{h_s - h_c}{x_s} \right) (x_s) \left(\frac{h_s + h_c}{2} \right) \overline{N^2_{A_1}} + \frac{\eta x_s}{h_s^2} \left(\frac{h_s' - h_s}{x_s'} \right) (x_s') \left(\frac{h_s' + h_s}{2} \right) \overline{N^2_{A_2}}, \tag{A3}$$

$$= \frac{\eta x_s}{2} \left(1 - \frac{h_c^2}{h_s^2} \right) \overline{N^2_{A_1}} + \frac{\eta N^2 x_s}{2} \left(\frac{h_s'^2}{h_s^2} - 1 \right) \overline{N^2_{A_2}}, \tag{A4}$$

$$= \frac{\eta x_s}{2} \frac{h_c}{h_s} \left[\left(\frac{h_s}{h_c} - \frac{h_c}{h_s} \right) \overline{N^2_{A_1}} + \left(\frac{h_s'^2}{h_s} - h_s \right) \frac{\overline{N^2_{A_2}}}{h_c} \right]. \tag{A5}$$

Here, $\overline{N^2_{A_1}}$ and $\overline{N^2_{A_2}}$ are the average N^2 over areas A_1 and A_2, respectively. Because $h_s^2 > h_s \geq h_c$, the term in the square brackets in Eq. (A5) that contains the dependency on the stratification is always positive. Also, notably, x_s' is eliminated except for in the correction term $\langle N^2 \rangle_{A_2}$, so the horizontal extent of $\tilde{F}_B$ over the slope does not appear in the approximation, which is perhaps why $\langle \tilde{F}_B \rangle_A$ (and subsequently, as we will show below, the magnitude of the baroclinic energy flux) is not sensitive to the slope width x_W.

Assuming that $\langle \mathcal{F}_{up} \rangle \propto \langle \tilde{F}_B \rangle_A$, from Eqs. (A1) and (A5), we get

$$\langle \mathcal{F}_{up} \rangle \propto \frac{1}{2} \left[\left(\frac{h_s}{h_c} - \frac{h_c}{h_s} \right) \overline{N^2_{A_1}} + \left(\frac{h_s'^2}{h_s} - h_s \right) \frac{\overline{N^2_{A_2}}}{h_c} \right] (\eta x_s) \frac{h_c}{h_s} \frac{\eta x_s}{h_c} \sqrt{\omega^2 - f^2}, \tag{A6}$$

$$\sim C_{\text{prop}} \frac{\langle \tilde{F}_B \rangle_A}{\langle \tilde{F}_B \rangle_A^0} \frac{\eta x_s}{h_c} \sqrt{\omega^2 - f^2}. \tag{A7}$$

Normalizing by $\langle \tilde{F}_B \rangle_A^0$ removes the dependency on the stratification, and we recover Eq. (37) with some proportionality constant C_{prop}.

Furthermore, the expression for body force in Eq. (21) assumes that at the shelf break, the barotropic cross-shore current is $u_{\text{bt}} = (Q/h_s)\exp(-i\omega t)$. Plugging this expression into Eq. (A7), we obtain the dependency of baroclinic energy flux on this velocity with $\tilde{C}_{\text{prop}}$ now including the term in the square brackets in Eq. (A6):

$$\langle \mathcal{F}_{up} \rangle \propto \tilde{C}_{\text{prop}} \frac{u_{\text{bt}}^2 h_s}{\langle \tilde{F}_B \rangle_A^0} \sqrt{\omega^2 - f^2}. \tag{A8}$$

REFERENCES

Alford, M. H., 2003: Redistribution of energy available for ocean mixing by long-range propagation of internal waves. *Nature*, **423**, 159–162, https://doi.org/10.1038/nature01628.

Baines, P. G., 1973: The generation of internal tides by flat-bump topography. *Deep-Sea Res. Oceanogr. Abstr.*, **20**, 179–205, https://doi.org/10.1016/0011-7471(73)90050-8.

——, 1982: On internal tide generation models. *Deep-Sea Res.*, **29A**, 307–338, https://doi.org/10.1016/0198-0149(82)90098-X.

Barbot, S., F. Lyard, M. Tchilibou, and L. Carrere, 2021: Background stratification impacts on internal tide generation and abyssal propagation in the western equatorial Atlantic and the Bay of Biscay. *Ocean Sci.*, **17**, 1563–1583, https://doi.org/10.5194/os-17-1563-2021.

Bell, T. H., Jr., 1975: Topographically generated internal waves in the open ocean. *J. Geophys. Res.*, **80**, 320–327, https://doi.org/10.1029/JC080i003p00320.

Cacchione, D. A., L. F. Pratson, and A. S. Ogston, 2002: The shaping of continental slopes by internal tides. *Science*, **296**, 724–727, https://doi.org/10.1126/science.1069803.

Carasso, A., 1969: Finite-difference methods and the eigenvalue problem for nonselfadjoint Sturm-Liouville operators. *Math. Comput.*, **23**, 717–729, https://doi.org/10.1090/S0025-5718-1969-0258291-7.

Chapman, D. C., and M. C. Hendershott, 1982: Shelf wave dispersion in a geophysical ocean. *Dyn. Atmos. Oceans*, **7**, 17–31, https://doi.org/10.1016/0377-0265(82)90003-3.

Chen, Z., J. Xie, J. Xu, Y. He, and S. Cai, 2017: Selection of internal wave beam directions by a geometric constraint provided by topography. *Phys. Fluids*, **29**, 066602, https://doi.org/10.1063/1.4984245.

Chuang, W.-S., and D.-P. Wang, 1981: Effects of density front on the generation and propagation of internal tides. *J. Phys. Oceanogr.*, **11**, 1357–1374, https://doi.org/10.1175/1520-0485(1981)011<1357:EODFOT>2.0.CO;2.

Craig, P. D., 1987: Solutions for internal tidal generation over coastal topography. *J. Mar. Res.*, **45**, 83–105, https://doi.org/10.1357/002224087788400954.

Dale, A. C., and T. J. Sherwin, 1996: The extension of baroclinic coastal-trapped wave theory to superinertial frequencies. *J. Phys. Oceanogr.*, **26**, 2305–2315, https://doi.org/10.1175/1520-0485(1996)026<2305:TEOBCT>2.0.CO;2.

——, J. M. Huthnance, and T. J. Sherwin, 2001: Coastal-trapped waves and tides at near-inertial frequencies. *J. Phys. Oceanogr.*, **31**, 2958–2970, https://doi.org/10.1175/1520-0485(2001)031<2958:CTWATA>2.0.CO;2.

Dauxois, T., A. Didier, and E. Falcon, 2004: Observation of near-critical reflection of internal waves in a stably stratified fluid. *Phys. Fluids*, **16**, 1936–1941, https://doi.org/10.1063/1.1711814.

de Lavergne, C., S. Falahat, G. Madec, F. Roquet, J. Nycander, and C. Vic, 2019: Toward global maps of internal tide energy sinks. *Ocean Modell.*, **137**, 52–75, https://doi.org/10.1016/j.ocemod.2019.03.010.

Drake, H. F., X. Ruan, J. Callies, K. Ogden, A. M. Thurnherr, and R. Ferrari, 2022: Dynamics of eddying abyssal mixing layers over sloping rough topography. *J. Phys. Oceanogr.*, **52**, 3199–3219, https://doi.org/10.1175/JPO-D-22-0009.1.

Duda, T. F., W. G. Zhang, and Y.-T. Lin, 2012: Studies of internal tide generation at a slope with nonlinear and linearized simulations: Dynamics and implications for ocean acoustics. *Proc. 2012 Oceans*, Hampton Roads, VA, Institute of Electrical and Electronics Engineers, 1–6.

Early, J. J., M. P. Lelong, and K. S. Smith, 2020: Fast and accurate computation of vertical modes. *J. Adv. Model. Earth Syst.*, **12**, e2019MS001939, https://doi.org/10.1029/2019MS001939.

Egbert, G. D., and S. Y. Erofeeva, 2002: Efficient inverse modeling of barotropic ocean tides. *J. Atmos. Oceanic Technol.*, **19**, 183–204, https://doi.org/10.1175/1520-0426(2002)019<0183:EIMOBO>2.0.CO;2.

Ferrari, R., A. Mashayek, T. J. McDougall, M. Nikurashin, and J.-M. Campin, 2016: Turning ocean mixing upside down. *J. Phys. Oceanogr.*, **46**, 2239–2261, https://doi.org/10.1175/JPO-D-15-0244.1.

Feucher, C., G. Maze, and H. Mercier, 2019: Subtropical mode water and permanent pycnocline properties in the world ocean. *J. Geophys. Res. Oceans*, **124**, 1139–1154, https://doi.org/10.1029/2018JC014526.

Fructus, D., M. Carr, J. Grue, A. Jensen, and P. A. Davies, 2009: Shear-induced breaking of large internal solitary waves. *J. Fluid Mech.*, **620**, 1–29, https://doi.org/10.1017/S0022112008004898.

Garrett, C., and T. Gerkema, 2007: On the body-force term in internal-tide generation. *J. Phys. Oceanogr.*, **37**, 2172–2175, https://doi.org/10.1175/JPO3165.1.

——, and E. Kunze, 2007: Internal tide generation in the deep ocean. *Annu. Rev. Fluid Mech.*, **39**, 57–87, https://doi.org/10.1146/annurev.fluid.39.050905.110227.

Gayen, B., and S. Sarkar, 2011a: Boundary mixing by density overturns in an internal tidal beam. *Geophys. Res. Lett.*, **38**, L14608, https://doi.org/10.1029/2011GL048135.

——, and ——, 2011b: Direct and large-eddy simulations of internal tide generation at a near-critical slope. *J. Fluid Mech.*, **681**, 48–79, https://doi.org/10.1017/jfm.2011.170.

GEBCO Compilation Group, 2020: GEBCO_2020 grid. National Oceanography Centre, accessed 20 September 2023, https://doi.org/10.5285/a29c5465-b138-234d-e053-6c86abc040b9.

Gekeler, E., 1974: On the eigenvectors of a finite-difference approximation to the Sturm-Liouville eigenvalue problem. *Math. Comput.*, **28**, 973–979, https://doi.org/10.1090/S0025-5718-1974-0356524-1.

Gerkema, T., 2001: Internal and interfacial tides: Beam scattering and local generation of solitary waves. *J. Mar. Res.*, **59**, 227–255, https://doi.org/10.1357/002224001762882646.

——, and H. van Haren, 2012: Absence of internal tidal beams due to non-uniform stratification. *J. Sea Res.*, **74**, 2–7, https://doi.org/10.1016/j.seares.2012.03.008.

——, F.-P. A. Lam, and L. R. M. Maas, 2004: Internal tides in the Bay of Biscay: Conversion rates and seasonal effects. *Deep-Sea Res. II*, **51**, 2995–3008, https://doi.org/10.1016/j.dsr2.2004.09.012.

——, C. Staquet, and P. Bouruet-Aubertot, 2006: Decay of semi-diurnal internal-tide beams due to subharmonic resonance. *Geophys. Res. Lett.*, **33**, L08604, https://doi.org/10.1029/2005GL025105.

Gheorghiu, C.-I., and B. Zinsou, 2019: Analytic vs. numerical solutions to a Sturm-Liouville transmission eigenproblem. *J. Numer. Anal. Approx. Theory*, **48**, 159–174, https://doi.org/10.33993/jnaat482-1201.

Griffiths, S. D., and R. H. J. Grimshaw, 2007: Internal tide generation at the continental shelf modeled using a modal decomposition: Two-dimensional results. *J. Phys. Oceanogr.*, **37**, 428–451, https://doi.org/10.1175/JPO3068.1.

Grisouard, N., and C. Staquet, 2010: Numerical simulations of the local generation of internal solitary waves in the Bay of Biscay. *Nonlinear Processes Geophys.*, **17**, 575–584, https://doi.org/10.5194/npg-17-575-2010.

Haidvogel, D. B., H. G. Arango, K. Hedstrom, A. Beckmann, P. Malanotte-Rizzoli, and A. F. Shchepetkin, 2000: Model evaluation experiments in the North Atlantic Basin: Simulations in nonlinear terrain-following coordinates. *Dyn. Atmos. Oceans*, **32**, 239–281, https://doi.org/10.1016/S0377-0265(00)00049-X.

Hall, R. A., J. M. Huthnance, and R. G. Williams, 2013: Internal wave reflection on shelf slopes with depth-varying stratification. *J. Phys. Oceanogr.*, **43**, 248–258, https://doi.org/10.1175/JPO-D-11-0192.1.

Haney, R. L., 1991: On the pressure gradient force over steep topography in sigma coordinate ocean models. *J. Phys. Oceanogr.*, **21**, 610–619, https://doi.org/10.1175/1520-0485(1991)021%3C0610:OTPGFO%3E2.0.CO;2.

Hartharn-Evans, S. G., M. Carr, M. Stastna, and P. A. Davies, 2022: Stratification effects on shoaling internal solitary waves. *J. Fluid Mech.*, **933**, A19, https://doi.org/10.1017/jfm.2021.1049.

Huthnance, J. M., 1975: On trapped waves over a continental shelf. *J. Fluid Mech.*, **69**, 689–704, https://doi.org/10.1017/S0022112075001632.

——, 1978: On coastal trapped waves: Analysis and numerical calculation by inverse iteration. *J. Phys. Oceanogr.*, **8**, 74–92,

https://doi.org/10.1175/1520-0485(1978)008<0074:OCTWAA>2.0.CO;2.

——, 1981: Waves and currents near the continental shelf edge. *Prog. Oceanogr.*, **10**, 193–226, https://doi.org/10.1016/0079-6611(81)90004-5.

Katsumata, K., 2006: Two- and three-dimensional numerical models of internal tide generation at a continental slope. *Ocean Modell.*, **12**, 32–45, https://doi.org/10.1016/j.ocemod.2005.03.001.

Kelly, S. M., 2016: The vertical mode decomposition of surface and internal tides in the presence of a free surface and arbitrary topography. *J. Phys. Oceanogr.*, **46**, 3777–3788, https://doi.org/10.1175/JPO-D-16-0131.1.

——, and J. D. Nash, 2010: Internal-tide generation and destruction by shoaling internal tides. *Geophys. Res. Lett.*, **37**, L23611, https://doi.org/10.1029/2010GL045598.

——, ——, and E. Kunze, 2010: Internal-tide energy over topography. *J. Geophys. Res.*, **115**, C06014, https://doi.org/10.1029/2009JC005618.

——, N. L. Jones, and J. D. Nash, 2013: A coupled model for Laplace's tidal equations in a fluid with one horizontal dimension and variable depth. *J. Phys. Oceanogr.*, **43**, 1780–1797, https://doi.org/10.1175/JPO-D-12-0147.1.

Klymak, J. M., H. L. Simmons, D. Braznikov, S. Kelly, J. A. MacKinnon, M. H. Alford, R. Pinkel, and J. D. Nash, 2016: Reflection of linear internal tides from realistic topography: The Tasman continental slope. *J. Phys. Oceanogr.*, **46**, 3321–3337, https://doi.org/10.1175/JPO-D-16-0061.1.

Kunze, E., C. MacKay, E. E. McPhee-Shaw, K. Morrice, J. B. Girton, and S. R. Terker, 2012: Turbulent mixing and exchange with interior waters on sloping boundaries. *J. Phys. Oceanogr.*, **42**, 910–927, https://doi.org/10.1175/JPO-D-11-075.1.

Lahaye, N., and S. G. Llewellyn Smith, 2020: Modal analysis of internal wave propagation and scattering over large-amplitude topography. *J. Phys. Oceanogr.*, **50**, 305–321, https://doi.org/10.1175/JPO-D-19-0005.1.

Lamb, K. G., 2014: Internal wave breaking and dissipation mechanisms on the continental slope/shelf. *Annu. Rev. Fluid Mech.*, **46**, 231–254, https://doi.org/10.1146/annurev-fluid-011212-140701.

Legg, S., and A. Adcroft, 2003: Internal wave breaking at concave and convex continental slopes. *J. Phys. Oceanogr.*, **33**, 2224–2246, https://doi.org/10.1175/1520-0485(2003)033<2224:IWBACA>2.0.CO;2.

Lerczak, J. A., C. D. Winant, and M. C. Hendershott, 2003: Observations of the semidiurnal internal tide on the Southern California slope and shelf. *J. Geophys. Res.*, **108**, 3068, https://doi.org/10.1029/2001JC001128.

Lindzen, R. S., and H.-L. Kuo, 1969: A reliable method for the numerical integration of a large class of ordinary and partial differential equations. *Mon. Wea. Rev.*, **97**, 732–734, https://doi.org/10.1175/1520-0493(1969)097%3C0732:ARMFTN%3E2.3.CO;2.

Liu, K., J. Sun, C. Guo, Y. Yang, W. Yu, and Z. Wei, 2019: Seasonal and spatial variations of the M_2 internal tide in the Yellow Sea. *J. Geophys. Res. Oceans*, **124**, 1115–1138, https://doi.org/10.1029/2018JC014819.

Llewellyn Smith, S. G., and W. R. Young, 2002: Conversion of the barotropic tide. *J. Phys. Oceanogr.*, **32**, 1554–1566, https://doi.org/10.1175/1520-0485(2002)032<1554:COTBT>2.0.CO;2.

——, and ——, 2003: Tidal conversion at a very steep ridge. *J. Fluid Mech.*, **495**, 175–191, https://doi.org/10.1017/S0022112003006098.

MacKinnon, J. A., and Coauthors, 2017: Climate process team on internal wave–driven ocean mixing. *Bull. Amer. Meteor. Soc.*, **98**, 2429–2454, https://doi.org/10.1175/BAMS-D-16-0030.1.

Manabe, S., and J. Smagorinsky, 1967: Simulated climatology of a general circulation model with a hydrologic cycle II. Analysis of the tropical atmosphere. *Mon. Wea. Rev.*, **95**, 155–169, https://doi.org/10.1175/1520-0493(1967)095<0155:SCOAGC>2.3.CO;2.

Maugé, R., and T. Gerkema, 2008: Generation of weakly nonlinear nonhydrostatic internal tides over large topography: A multi-modal approach. *Nonlinear Processes Geophys.*, **15**, 233–244, https://doi.org/10.5194/npg-15-233-2008.

Mesinger, F., 1982: On the convergence and error problems of the calculation of the pressure gradient force in sigma coordinate models. *Geophys. Astrophys. Fluid Dyn.*, **19**, 105–117, https://doi.org/10.1080/03091928208208949.

Morozov, E. G., 1995: Semidiurnal internal wave global field. *Deep-Sea Res. I*, **42**, 135–148, https://doi.org/10.1016/0967-0637(95)92886-C.

Munk, W., and C. Wunsch, 1998: Abyssal recipes II: Energetics of tidal and wind mixing. *Deep-Sea Res. I*, **45**, 1977–2010, https://doi.org/10.1016/S0967-0637(98)00070-3.

Musgrave, R. C., 2019: Energy fluxes in coastal trapped waves. *J. Phys. Oceanogr.*, **49**, 3061–3068, https://doi.org/10.1175/JPO-D-18-0172.1.

Mysak, L. A., 1980: Topographically trapped waves. *Annu. Rev. Fluid Mech.*, **12**, 45–76, https://doi.org/10.1146/annurev.fl.12.010180.000401.

Nash, J. D., E. Kunze, J. M. Toole, and R. W. Schmitt, 2004: Internal tide reflection and turbulent mixing on the continental slope. *J. Phys. Oceanogr.*, **34**, 1117–1134, https://doi.org/10.1175/1520-0485(2004)034<1117:ITRATM>2.0.CO;2.

Papoutsellis, C. E., M. J. Mercier, and N. Grisouard, 2023: Internal tide generation from non-uniform barotropic body forcing. *J. Fluid Mech.*, **964**, A20, https://doi.org/10.1017/jfm.2023.358.

Rattray, M., Jr., 1960: On the coastal generation of internal tides. *Tellus*, **12A**, 54–62, https://doi.org/10.3402/tellusa.v12i1.9344.

——, 1969: Generation of the long internal waves at the continental slope. *Deep-Sea Res.*, **16**, 179–195.

Rayson, M. D., N. L. Jones, and G. N. Ivey, 2012: Temporal variability of the standing internal tide in the Browse basin, western Australia. *J. Geophys. Res.*, **117**, C06013, https://doi.org/10.1029/2011JC007523.

——, ——, and ——, 2019: Observations of large-amplitude mode-2 nonlinear internal waves on the Australian North West Shelf. *J. Phys. Oceanogr.*, **49**, 309–328, https://doi.org/10.1175/JPO-D-18-0097.1.

Shchepetkin, A. F., and J. C. McWilliams, 2003: A method for computing horizontal pressure-gradient force in an oceanic model with a nonaligned vertical coordinate. *J. Geophys. Res.*, **108**, 3090, https://doi.org/10.1029/2001JC001047.

Sherwin, T., and N. Taylor, 1989: The application of a finite difference model of internal tide generation to the NW European Shelf. *Deutsche Hydrografische Z.*, **42**, 151–167, https://doi.org/10.1007/BF02226292.

Sherwin, T. J., and N. K. Taylor, 1990: Numerical investigations of linear internal tide generation in the Rockall Trough. *Deep-Sea Res.*, **37A**, 1595–1618, https://doi.org/10.1016/0198-0149(90)90064-3.

——, V. I. Vlasenko, N. Stashchuk, D. R. G. Jeans, and B. Jones, 2002: Along-slope generation as an explanation for some unusually large internal tides. *Deep-Sea Res. I*, **49**, 1787–1799, https://doi.org/10.1016/S0967-0637(02)00096-1.

Sikirić, M. D., I. Janeković, and M. Kuzmić, 2009: A new approach to bathymetry smoothing in sigma-coordinate ocean

models. *Ocean Modell.*, **29**, 128–136, https://doi.org/10.1016/j.ocemod.2009.03.009.

Stammer, D., and Coauthors, 2014: Accuracy assessment of global barotropic ocean tide models. *Rev. Geophys.*, **52**, 243–282, https://doi.org/10.1002/2014RG000450.

Stevens, C. L., P. J. Sutton, and C. S. Law, 2012: Internal waves downstream of Norfolk Ridge, western Pacific, and their biophysical implications. *Limnol. Oceanogr.*, **57**, 897–911, https://doi.org/10.4319/lo.2012.57.4.0897.

Stewart, A. L., and A. F. Thompson, 2016: Eddy generation and jet formation via dense water outflows across the Antarctic continental slope. *J. Phys. Oceanogr.*, **46**, 3729–3750, https://doi.org/10.1175/JPO-D-16-0145.1.

St. Laurent, L., S. Stringer, C. Garrett, and D. Perrault-Joncas, 2003: The generation of internal tides at abrupt topography. *Deep-Sea Res. I*, **50**, 987–1003, https://doi.org/10.1016/S0967-0637(03)00096-7.

Suanda, S. H., and J. A. Barth, 2015: Semidiurnal baroclinic tides on the central Oregon inner shelf. *J. Phys. Oceanogr.*, **45**, 2640–2659, https://doi.org/10.1175/JPO-D-14-0198.1.

Tuerena, R. E., R. G. Williams, C. Mahaffey, C. Vic, J. A. M. Green, A. Naveira-Garabato, A. Forryan, and J. Sharples, 2019: Internal tides drive nutrient fluxes into the deep chlorophyll maximum over mid-ocean ridges. *Global Biogeochem. Cycles*, **33**, 995–1009, https://doi.org/10.1029/2019GB006214.

Vieira, G. S., and M. R. Allshouse, 2020: Internal wave boluses as coherent structures in a continuously stratified fluid. *J. Fluid Mech.*, **885**, A35, https://doi.org/10.1017/jfm.2019.993.

Wang, S., X. Chen, Q. Li, J. Wang, J. Meng, and M. Zhao, 2018: Scattering of low-mode internal tides at different shaped continental shelves. *Cont. Shelf Res.*, **169**, 17–24, https://doi.org/10.1016/j.csr.2018.09.010.

——, A. Cao, X. Chen, Q. Li, and J. Song, 2021: On the resonant triad interaction over mid-ocean ridges. *Ocean Modell.*, **158**, 101734, https://doi.org/10.1016/j.ocemod.2020.101734.

Wunsch, C., and R. Ferrari, 2004: Vertical mixing, energy, and the general circulation of the oceans. *Annu. Rev. Fluid Mech.*, **36**, 281–314, https://doi.org/10.1146/annurev.fluid.36.050802.122121.

Yankovsky, A. E., and T. Zhang, 2017: Scattering of a semidiurnal barotropic Kelvin wave into internal waves over wide continental shelves. *J. Phys. Oceanogr.*, **47**, 2545–2562, https://doi.org/10.1175/JPO-D-16-0284.1.

Zaron, E. D., and S. Elipot, 2021: An assessment of global ocean barotropic tide models using geodetic mission altimetry and surface drifters. *J. Phys. Oceanogr.*, **51**, 63–82, https://doi.org/10.1175/JPO-D-20-0089.1.

Zhang, T., and A. E. Yankovsky, 2016: On the nature of cross-isobath energy fluxes in topographically modified barotropic semidiurnal Kelvin waves. *J. Geophys. Res. Oceans*, **121**, 3058–3074, https://doi.org/10.1002/2015JC011617.